

Additional Topics on GNSS

Paul D. Groves

| | | |
|------|--|------|
| G.1 | GNSS Space and Control Segments | G-2 |
| | G.1.1 GPS | G-2 |
| | G.1.2 GLONASS | G-4 |
| | G.1.3 Galileo | G-4 |
| G.2 | GNSS Development History | G-5 |
| | G.2.1 GPS | G-5 |
| | G.2.2 GLONASS | G-6 |
| | G.2.3 Galileo | G-7 |
| | G.2.4 Other Systems | G-8 |
| G.3 | GNSS Signal Design Notes | G-8 |
| | G.3.1 Multiplexed BOC | G-8 |
| | G.3.2 Signal Multiplexing | G-10 |
| | G.3.3 Ranging Code Design | G-10 |
| G.4 | Satellite Position, Velocity, and Acceleration | G-11 |
| | G.4.1 Satellite and Range Acceleration | G-11 |
| | G.4.2 GLONASS Satellite Position and Velocity Calculation | G-13 |
| G.5 | Relativistic Frequency Shift | G-14 |
| G.6 | Receiver and Ranging Processor Design Notes | G-14 |
| | G.6.1 Postcorrelation Signal to Noise | G-14 |
| | G.6.2 BOC Tracking | G-15 |
| | G.6.3 Carrier-Power-to-Noise-Density Measurement | G-17 |
| G.7 | Range Error Corrections | G-19 |
| | G.7.1 Intersignal Timing Biases | G-19 |
| | G.7.2 Klobuchar Ionosphere Model | G-19 |
| | G.7.3 SBAS Ionosphere Model | G-20 |
| | G.7.4 WAAS Troposphere Delay Model | G-21 |
| | G.7.5 University of New Brunswick 3 Troposphere Delay Model | G-21 |
| G.8 | Navigation Processor | G-23 |
| | G.8.1 Estimating Interconstellation Timing Biases | G-23 |
| | G.8.2 Time Difference of Arrival across Satellites | G-26 |
| | G.8.3 Using Delta-Range Measurements | G-27 |
| | G.8.4 Signal Geometry with a Chip-Scale Atomic Clock | G-28 |
| G.9 | Integer Wavelength Ambiguity Resolution | G-29 |
| | G.9.1 Single-Epoch Float Solution | G-29 |
| | G.9.2 Filtered Float Solution | G-30 |
| | G.9.3 Correlation Properties of Geometry-Based Float Ambiguity Estimates | G-31 |
| | G.9.4 The LAMBDA Method | G-32 |
| | G.9.5 Ambiguity Validation | G-34 |
| | G.9.6 Properties of Wide-lane Measurements | G-34 |
| G.10 | Vector Tracking and Acquisition | G-35 |
| | G.10.1 Vector Phase Lock Loop | G-35 |
| | G.10.2 Collective Detection | G-35 |
| G.11 | Multipath and NLOS Mitigation | G-36 |
| | G.11.1 Multipath Mapping | G-36 |
| | G.11.2 Techniques for Reference Stations | G-36 |
| G.12 | Positioning using Ambiguous Pseudo-ranges | G-37 |
| G.13 | GNSS Repeaters | G-37 |
| | References | G-37 |

GNSS is described in detail in Chapters 8 to 10. This appendix presents a number of topics that could not be accommodated within those chapters. Section G.1 provides further information about the space and control segments. Section G.2 presents some historical notes on the development of the GNSS systems and describes some past features of GPS and GLONASS that are no longer applicable. Section G.3 provides further information on the signal designs. Section G.4 presents additional information on satellite position, velocity, and acceleration determination. Section G.5 summarizes the relativistic frequency shift. Section G.6 presents some receiver and ranging processor design notes covering postcorrelation signal to noise, BOC signal tracking, and C/N_0 measurement. Section G.7 describes the calculation of intersignal timing biases and presents models for calculating the ionosphere and troposphere propagation delays. Section G.8 describes alternative implementations of the position and signal geometry calculations. Section G.9 provides more details on integer wavelength ambiguity resolution for carrier-phase-based differential and relative positioning. Section G.10 discusses advanced vector tracking and acquisition techniques. Section G.11 discusses further multipath and NLOS reception mitigation techniques. Section G.12 discusses positioning using ambiguous pseudo-range measurements. Finally, Section G.13 discusses the use of GNSS repeaters for indoor positioning.

G.1 GNSS Space and Control Segments

This section provides more detailed information on the GPS, GLONASS, and Galileo space and control segments. Detailed information on Beidou was not available at the time of writing. All GNSS satellites incorporate redundant equipment, enabling them to continue operation when something fails. For example, multiple frequency standards to drive the satellite clock are standard equipment. Satellites use momentum wheels to keep their broadcast and receive antennae pointing towards the Earth and their solar panels pointing towards the sun. The panels may also be rotated. Otherwise, the orientation would remain fixed with respect to inertial space. Momentum wheels operate by conservation of angular momentum; the satellite turns in the opposite direction to the wheel. Thrusters are used to keep the satellites in the correct orbit and move them within that orbit where required. The last fuel is used to move the satellite to a parking orbit, away from the operational satellites, at the end of its life.

G.1.1 GPS

GPS satellites are referred to by two different numbering schemes. The space vehicle number (SVN) is unique to each satellite, while the PRN number denotes the set of ranging codes that the satellite is transmitting. Satellites can change PRN number, but do not change SVN number. GPS signals are transmitted over a beam about 28° , covering the whole Earth. A slightly higher power is used at the edge of the beam to compensate for the distance traveled by the signals being larger at the edge as Figure G.1 illustrates. This ensures a roughly uniform received signal strength over the reception area on the Earth's surface. All current satellites also use momentum management to maintain their orbits with less intervention from the control segment.

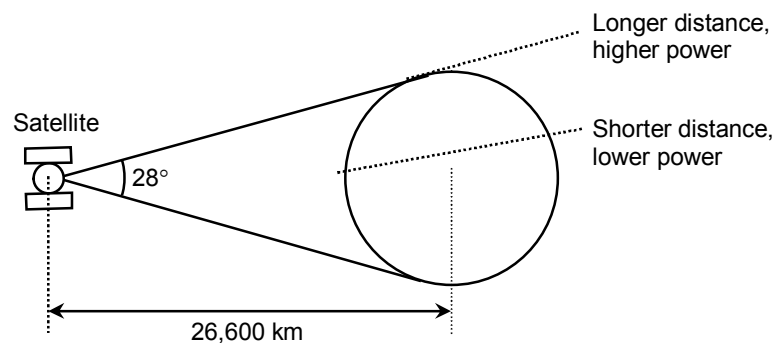


Figure G.1 GPS satellite coverage.

Table 8.1 lists the present and planned generations of GPS satellite. Successive designs are larger and more powerful. The Block II and IIA satellites, made by Rockwell International (now part of Boeing) have a design life of 7.5 years, though most have lasted much longer. They are each equipped with two cesium and two rubidium frequency standards. More details can be found in [1].

The Block IIR, ‘replenishment’, satellites and subsequent designs incorporate automatic navigation (Autonav) feature, which enables the navigation data to be updated independently of the control segment using inter-satellite ranging measurements. Three rubidium frequency standards are used. The Block IIR and Block IIR-M, “modernized replenishment” satellites were made by Lockheed Martin and have a design life of 10 years; again, many have lasted longer. The Block IIF, “follow-on”, satellites are made by Boeing and have a design life of 12.7 years. They use rubidium and cesium frequency standards.

The Block III satellites will introduce further new signals, broadcast some signals, such as M-code, at a higher power and incorporate a flex power capability whereby the powers of different signals may be varied. The design life will be 15 years. At the time of writing, it was proposed to deploy Block III in three generations, comprising 8 Block IIIA, 8 Block IIIB, and 16 Block IIIC satellites. However, this is subject to change. The Block IIIA satellites are being built by Lockheed Martin. The capability to relay control segment commands from one satellite to another, known as cross linking, is proposed for the Block IIIB satellites. For the Block IIIC satellites, the capability to broadcast a ‘spot beam’ of additional M-code signals over a limited area is planned. This will provide a received signal strength 20 dB higher than the global M-code signal. The spot beam will broadcast in both the L1 and L2 bands using different PRN codes from the global M-code signal.

GPS satellites can transmit an additional signal on 1381.05 MHz, known as L3. This is used by the Nuclear Detonation Detection System; it is not designed for navigation [2]. The uplink frequency, used for transmissions from the control segment to the satellites, is 1783.74 MHz.

The GPS Operational Control Segment (OCS) currently comprises a master control station (MCS) near Colorado Springs, Colorado, an alternate MCS at Vandenberg Air Force Base in California, 16 monitor stations (including those operated by the National Geospatial-Intelligence Agency), and 12 uplink stations (including the Air Force Satellite Control Network (AFSCN) stations). The monitor stations are located at

- | | |
|------------------------------|--------------------------------|
| • Adelaide, Australia | • Hermitage, England |
| • Ascension, South Atlantic | • Kwajalein, Pacific Ocean |
| • Buenos Aires, Argentina | • Manama, Bahrain, Middle East |
| • Cape Canaveral, USA | • Oscan, South Korea |
| • Colorado Springs, USA | • Pretoria, South Africa |
| • Diego Garcia, Indian Ocean | • Quito, Ecuador |
| • Fairbanks, Alaska, USA | • Washington, D.C., USA |
| • Hawaii, Pacific Ocean | • Wellington, New Zealand |

An additional NGA site on Tahiti in the Pacific Ocean was not equipped with a GPS monitor station at the time of writing. The uplink stations are located at

- | | |
|---|-----------------------------------|
| • Ascension, South Atlantic | • Hawaii, Pacific Ocean |
| • Cape Canaveral, USA (2 stations) | • Kwajalein, Pacific Ocean |
| • Colorado Springs, USA | • RAF Oakhanger, England |
| • Diego Garcia, Indian Ocean (2 stations) | • Thule Air Base, Greenland |
| • Guam, South Pacific | • Vandenberg AFB, California, USA |

A new series of control segment enhancements, known as OCX are planned for introduction with the launch of the Block III satellites. This will include MCS software upgrades to handle Block III satellites, support all of the new features of the CNAV and MNAV messages, and increase the number of controllable satellites from 32 to 63. Note,

however that the current ITU frequency filing and the number of available C/A codes limits the number of transmitting satellites to 36. The first of four phases of the OCX program will be completed in 2016-17.

G.1.2 GLONASS

Table 8.2 lists the present and planned generations of GLONASS satellite. GLONASS-M satellites have a design life of 7 years and use cesium frequency standards. GLONASS-K satellites have a design life of at least 10 years, improved frequency standards, and a more modern satellite bus.

The GLONASS ground-based control complex (GBCC) is in the process of being modernized. There are two control centers near Moscow, at Krasnoznamensk (formerly known as Golitsyno-2) and Schelkovo. Five telemetry, tracking, and control (TT&C) stations are located at Komsomolsk, Schelkovo, St Petersburg, Ussurlysk, and Yenisselsk, all in Russia. These uplink commands to the satellites and monitor the GLONASS signals. Originally, the monitor station measurements were only used to calibrate the receiver clocks, with satellite orbits determined from radar tracking by the TT&C stations every 10 to 14 orbits. Laser tracking stations were used to periodically calibrate the radar tracking [3].

At the time of writing, GLONASS was changing to determining the satellite orbits from the GLONASS ranging signals using a network of monitor stations [4]. Monitor stations are located at the control centers; the TT&C stations; Murmansk, Ullan-Ude, Vorkuta, Yakutsk, and Zelenchuk in Russia; and Nurek in Tajikistan.

G.1.3 Galileo

The Galileo space and ground segments are being developed in three phases: in-orbit validation (IOV), initial operational capability, and full operational capability. Table G.1 shows the total number of satellites, TT&C stations, uplink stations and Galileo Sensor Stations (GSSs), deployed by the end of each phase [5]. Note that a GSS is a monitor station.

Table G.1 Galileo Space and Ground Segment Deployment Phases

| <i>Phase</i> | <i>Number of Satellites</i> | <i>Number of TT&C Stations</i> | <i>Number of Uplink Stations</i> | <i>Number of GSSs</i> |
|--------------|-----------------------------|------------------------------------|----------------------------------|-----------------------|
| IOV | 4 | 2 | 5 | 9 |
| IOC | 14 + 4 = 18 | 2 + 2 = 4 | 1 + 5 = 6 | 7 + 9 = 16 |
| FOC | 9 + 18 = 27 (+ 3 spares) | 1 + 4 = 5 | 3 + 6 = 9 | 18 + 16 = 34 |

The GIOVE-A and GIOVE-B test satellites were built by Surrey Satellite Technology Ltd. (SSTL) and EADS Astrium, respectively. The four IOV satellites, the first of the permanent constellation, have been built by EADS Astrium and were launched in 2012. The next 22 satellites are being built by OHB with the navigation payload subcontracted to SSTL. Funding for the final four planned satellites had not been secured at the time of writing. Each Galileo satellite has two rubidium frequency standards and two passive hydrogen masers.

The Galileo ground segment is partitioned into two separate systems, a Ground Control Segment (GCS) and Ground Mission Segment (GMS). Essentially, the GCS controls the satellite hardware, while the GMS controls the navigation service, including generation of the navigation data message content and integrity alerts. The GCS control center is located at Oberpfaffenhofen near Munich in Germany, while the GMS control center is at Fucino Space Center in Italy. Each control center also acts as a backup for the other. Batch processing over a ten minute cycle is used to determine the precise orbit and clock offset of each satellite, while a separate Integrity Processing Function (IPF) will provide instant alerts of satellite signal failures [6].

The following stations are being commissioned for the IOV phase of development:

- Fucino, Italy (GSS);
- Kiruna, Sweden (TT&C)
- Kourou, French Guyana (TT&C, uplink, GSS);

- Noumea, New Caledonia in the South Pacific (uplink, GSS);
- Papeeta, Tahiti in the Pacific Ocean (uplink, GSS);
- Redu, Belgium (GSS);
- Reunion in the, Indian Ocean (uplink, GSS);
- Svalbard in the Norwegian Arctic (uplink, GSS);
- Troll, Antarctica (GSS);
- Washington D.C., USA (GSS).

The additional TT&C stations at FOC will be at Noumea, Papeeta, and Reunion. Sites under consideration for further GSS include:

- | | |
|--------------------------------------|--|
| • Ascension, South Atlantic | • Kerguelen, Indian Ocean |
| • Azores or Canaries, NE Atlantic | • Perth, Australia |
| • Cordoba, Argentina | • Reykjavik, Iceland |
| • Easter Island, South Pacific | • Riyadh, Saudi Arabia |
| • Falklands, South Atlantic | • Saint Pierre and Miquelon, NW Atlantic |
| • Guam, South Pacific | • South Korea |
| • Hartebeesthoek, South Africa | • Terre Adélie, Antarctica |
| • Hawaii, Pacific Ocean | • Wainwright, Alaska, USA |
| • Jan Mayen Island, Norwegian Arctic | • Washington, D.C., USA |

G.2 GNSS Development History

This section provides some historical notes on the development of GPS, GLONASS, Galileo, and other systems. It also describes some early features of GPS and GLONASS that no longer apply today.

G.2.1 GPS

From the mid 1960s to the mid 1970s, the United States Navy, Air Force, and Army all operated separate satellite navigation research and development programs. The Navy program was Timation, looking at a successor to the already operational Transit system; the Air Force program was 621B; and the Army program was Tactical Navsat. A joint service committee, known as the Navigation Satellite Executive Steering Group (NAVSEG), was convened in 1969 by the Office of the Secretary of Defense (OSD) to consolidate the requirements and development programs of each military service into a joint Defense Navigation Satellite System (DNSS) [7].

The DNSS became NAVSTAR GPS, the controlling body of which, the Joint Program Office (JPO), was formed in 1973. This replaced the earlier programs with a joint development program led by the Air Force [8, 9]. The JPO became the GPS Wing in 2006 and then the GPS Directorate in 2010. The NAVSTAR GPS program built primarily on the 621B program with some inputs from the Transit and Timation programs [10]. Key challenges in the development of the GPS system included optimizing the signal structure, developing atomic clocks suitable for extended deployment in space, predicting the satellite orbits rapidly and accurately, demonstrating satellite longevity, and developing a range of user equipment when digital technology was in its infancy [11].

The first operational prototype GPS satellite was launched in 1978. This was one of 10 Block I satellites that were used for system testing and concept validation, noting that this was not a sufficient number for continuous global coverage. The last Block I satellite was launched in 1985. Unlike the satellites for the operational system, the Block I satellites occupied orbits inclined at 63° to the equator and the constellation was optimized to give best coverage over the test site at Yuma, Arizona [12]. Even at Yuma, there was only sufficient satellite availability to form a single-epoch navigation solution at certain times of day. However, the Block I constellation was used for surveying and geodesy applications as, with observations over several hours, sufficient satellites could be observed to determine the position of static objects. Note that at least two satellites must be tracked at one time to cancel out the receiver

clock offset and obtain a hyperboloid surface of position. The last Block I satellite was decommissioned in 1995.

Nine Block II satellites were launched in 1989 and 1990 followed by 19 Block IIA satellites between 1990 and 1997. These were the first “production” satellites that would form the operational GPS system. Unlike subsequent designs, the Block II satellites did not use momentum management. Initial operational capability was declared at the end of 1993 and full operational capability attained at the end of 1994 [8, 9].

During the 1990s, the accuracy of the SPS was deliberately degraded to the order of 100m using a technique called Selective Availability (SA) [13]. This was done in order to deny precise positioning to hostile forces. SA was implemented by perturbing the satellite clock offsets. Encrypted corrections were included in the broadcast navigation data that could be decoded by military PPS users, but not by SPS users. The time correlation properties of the clock perturbations were deliberately chosen to disrupt INS/GPS integration using uncorrected GPS measurements. However, SA could be circumvented using differential GPS (DGPS) (Section 10.1), while hostile use of GPS can be denied on a local basis using jamming techniques. At the same time, GPS had become an important utility for an increasing number of civil and commercial applications. SA was therefore deactivated on May 1, 2000. The capability was initially retained, but is not available on the latest Block III satellites.

Deactivation of SA was the first step in the GPS modernization process that began at the end of the 1990s. This recognized that GPS, while originally conceived as a military system, had become an important part of the civil national (and international) infrastructure and a major contributor to the economy. Furthermore, Europe was announcing plans to launch a civil GNSS promising much higher performance. New signals were therefore introduced to improve the SPS and provide PPS users with spectrally separated signals. The first of the new signals, L2C and M-code were introduced with the Block IIR-M satellites, the first of which was launched in 2005. The first L5 signals were broadcast in 2009 from SVN-49, a specially modified Block IIR-M satellite. However, the modifications resulted in the transmission of faulty L1 and L2 signals, so this satellite was never fully commissioned. A frequency allocation between 1260 and 1300 MHz, known as L6, was also obtained. However, this was not taken up and has now expired.

The modernization program also includes improvements to the space and control segments, which benefit all user communities. The original GPS control segment had only 5 monitor stations (Hawaii, Colorado, Ascension, Diego Garcia, and Kwajalien) and 4 uplink stations (Cape Canaveral, Ascension, Diego Garcia, and Kwajalien). An extra monitor station at Cape Canaveral was later added. By incorporating National Geospatial-Intelligence Agency (NGA) stations, the monitoring network was extended to 12 stations in 2005 [14], with a further extension to 16 completed by 2009.

In September 2007, the MCS software was upgraded. At the same time, the number of GPS uplink stations was increased from 4 to 12 by incorporating the capability to command satellites through the AFSCN. These measures were part of the Legacy Accuracy Improvement Initiative (L-AII) [14]. Due to a combination of the control segment developments and the improving stability of the clocks deployed on each generation of satellites the signal in space error (combining ephemeris and residual satellite clock errors) has reduced from around 2.3m in the mid 1990s to 0.9m in 2009.

The GPS modernization program was ongoing at the time of writing. Future plans are described in Chapter 8 and in Section G.1 of this appendix.

G.2.2 GLONASS

GLONASS was developed as a military navigation system by the USSR from the mid 1970s, in parallel to GPS. The first satellite was launched in 1982. Following the dissolution of the Soviet Union, GLONASS development was continued by Russia, with a full satellite constellation achieved briefly in 1995. However, due to financial problems and the relatively-short lifetime of the original generation of satellites, the constellation was then allowed to decay, reaching a nadir of 6 satellites in 2001. In August 2001, a modernization program was

instigated, rebuilding the constellation, introducing new signals, and updating the control segment. India became a partner in the operation of GLONASS in December 2004 [4], but subsequently went on to develop its own regional GNSS-based satellite navigation system, IRNSS. IOC with 18 satellites was achieved in 2010, with a full 24-satellite constellation operational in 2011.

The original generation of GLONASS satellites had a design life of only three years, but lasted for an average of 4.5 years in practice. More than 80 of the original GLONASS satellites were launched between 1982 and 2007. The civil “C/A-code” signal was transmitted on the L1 frequency only, while military signals were transmitted on two frequencies. All GLONASS signals were FDMA.

Until September 1993, each satellite was allocated its own channel, numbered from 1 to 24. After that, only channels 1 to 12 were used to limit interference to radio astronomy, with satellites in opposite slots in the same orbital plane sharing the same channels. A further migration to channels –7 to +6 was completed in 2008 to further reduce interference to radio astronomy.

The first of the modernized GLONASS-M satellites was launched in 2003, featuring civil FDMA signals on two frequencies, a higher accuracy clock, and a longer design life. The first CDMA signals (on the L3 frequency) were broadcast in 2011 from the first GLONASS-K prototype satellite.

As with GPS, the GLONASS modernization program is ongoing and future plans are discussed in Chapter 8 and in Section G.1 of this appendix.

G.2.3 Galileo

Development of the Galileo satellite navigation system was initiated in 1999 by the European Union and European Space Agency. The Galileo Joint Undertaking (GJU) was formed to design the system. The Galileo open service was originally designed to provide much better performance than GPS SPS offered at the time. However with GPS modernization, performance differences between the two systems are likely to be small. The first test satellite, Galileo In-Orbit Validation Element (GIOVE)-A, built by SSTL, was launched on December 28th, 2005. At the beginning of 2007, the GJU was replaced by the Galileo Supervisory Authority (GSA), which then became the European GNSS Agency in November 2010. The second test satellite, GIOVE-B, built by EADS Astrium, was launched on April 27th, 2008. The first four satellites of the permanent constellation for the in-orbit validation (IOV) phase of development were launched in 2012.

The origin plan was to deploy and operate Galileo as a public private partnership (PPP). Under the PPP plan, 2/3 of the funding would be private. This would then be recouped through user charges for the proposed commercial services. It was envisaged that the commercial services would provide improved accuracy for those users willing to pay subscription charges. Encrypted signals in a third frequency band (E6) would provide greater protection against interference and improved carrier-phase positioning (see Section 10.2.1). In addition, higher-precision ephemeris and satellite clock parameters and local differential corrections could be broadcast. Commercial services could also be used to provide paying subscribers with a financially-guaranteed service level. The tendering process for a commercial concession to implement Galileo as a PPP began in February 2004. However, no viable business model was identified and the PPP concept was abandoned in June 2007.

Galileo deployment continued as a purely public-funded initiative with extra funding (from the EU’s agriculture and administration budgets) agreed in November 2007. The scope of the project was subsequently reduced with an initial deployment of only 18 satellites (now increased to 26) and only the open, PRS and search-and-rescue services implemented. Tenders for the space and ground segments were awarded in 2009-10. However, the future of both the safety-of-life and commercial services remains uncertain at the time of writing.

Note that during the design phase, the term ‘Galileo local component’ was adopted to encompass GBAS and other locally-based enhancements to the global Galileo service, while SBAS and other regional augmentation system were described as regional components of Galileo. This terminology has not been used in recent years.

G.2.4 Other Systems

The original Beidou system was a radio determination satellite service. This operated on a different principle to GNSS and is described in Section F.2.1 of Appendix F, also on CD. The first GNSS Beidou satellite was launched in 2007.

SBAS was originally conceived in the early 1990s [15, 16], adding wide-area DGPS to the GPS integrity channel concept, proposed in the 1980s [17]. WAAS development started in 1994 and became available for non-safety-critical use within the conterminous United States and parts of Alaska in August 2000. It was then certified for safety-of-life use in July 2003. Coverage was expanded to include most of Canada and Mexico in 2008.

EGNOS was first proposed in 1994. Initial operations, on a test basis, started in July 2005. The official launch was in October 2009 with certification for safety-of-life applications achieved in March 2011.

The first MSAS satellite was launched in February 2005 and the system was commissioned for aviation use in September 2007. Two GAGAN satellites were successfully launched in 2011 and 2012 with a third satellite scheduled for launch in 2013-14. The first satellite broadcasting SDCM was launched in 2011. A Nigerian plan to implement SBAS was delayed after the in-orbit failure of NigComSat-1 in 2008. The replacement satellite, NigComSat-1R, was successfully launched in December 2011, but the status of the SBAS program was not known at the time of writing.

GBAS development began with the development and demonstration of the integrity beacon landing system (IBLS) by Stanford University in the early 1990s. The Federal Aviation Administration (FAA)’s LAAS program then began in the mid 1990s [18]. A Honeywell implementation was approved for use in September in 2009 by the FAA. As of August 2010, the FAA has abandoned the term LAAS in favor of GBAS.

Australia developed a hybrid augmentation system, known as the Ground-based Regional Augmentation System (GRAS) [19]. It combined an SBAS-like reference station network with a network of ground-based VHF transmitters, mostly located near airfields, each broadcasting to airborne users within a radius of about 350 km. GRAS was commissioned in 2005, but was subsequently cancelled in 2008.

G.3 GNSS Signal Design Notes

This section presents additional information on GNSS signal design, including multiplexed BOC, signal multiplexing, and ranging code design.

G.3.1 Multiplexed BOC

An MBOC signal replaces the simple square-wave subcarrier function, $S(t)$, of a basic BOC signal (see Section 8.3.1) with a more complex function. MBOC is currently used in GNSS as a way of combining a higher-powered $\text{BOC}_s(1,1)$ signal with a lower-powered $\text{BOC}_s(6,1)$ signal. For both the GPS L1C-d + L1C-p combined signal and the Galileo E1-B + E1-C combined signal, the $\text{BOC}_s(1,1)$ component has 10 times the power of the $\text{BOC}_s(6,1)$ component. However, the implementations for the two systems are very different.

For GPS, the L1C-d signal is $\text{BOC}_s(1,1)$ only, while a time-multiplexed BOC is implemented for L1C-p. For TMBOC, the total subcarrier function is a repeating sequence of 33 segments of equal length. Segments 1, 5, 7, and 30 each comprise six 6.138-MHz square waveforms, while the remaining segments each comprise a single 1.023-MHz square waveform. Figure G.2 illustrates this.

For Galileo, a composite BOC modulation is used, which is the sum of the $\text{BOC}_s(1,1)$ and $\text{BOC}_s(6,1)$ components for the pilot signal, E1-C, and the difference for the data-modulated signal, E1-B [20, 21]. This may be written as

$$\begin{aligned}
S_{E1B}(t) &= \sqrt{\frac{10}{11}} S_{BOCs(1,1)}(t) - \sqrt{\frac{1}{11}} S_{BOCs(6,1)}(t) \\
S_{E1C}(t) &= \sqrt{\frac{10}{11}} S_{BOCs(1,1)}(t) + \sqrt{\frac{1}{11}} S_{BOCs(6,1)}(t)
\end{aligned} \tag{G.1}$$

where $S_{BOCs(1,1)}(t)$ is a 1.023-MHz square waveform in-phase with a 1.023-Mchip s^{-1} spreading code and $S_{BOCs(6,1)}(t)$ is a 6.138-MHz square waveform in-phase with the same spreading code. Figure G.3 illustrates this.

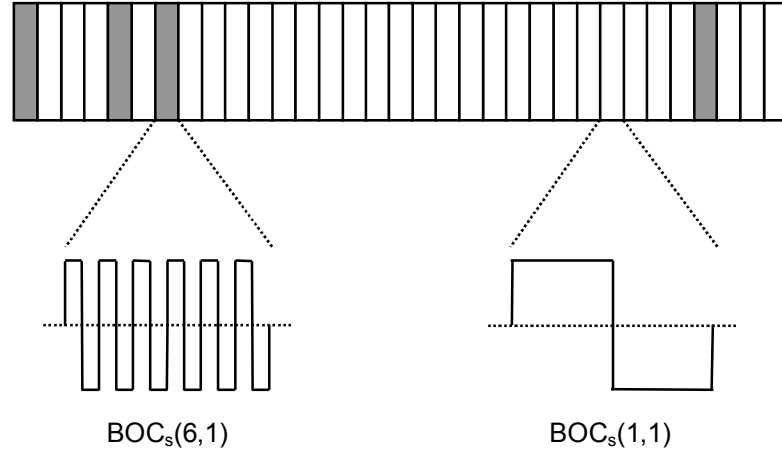


Figure G.2 TmBOC subcarrier function (after [20]).

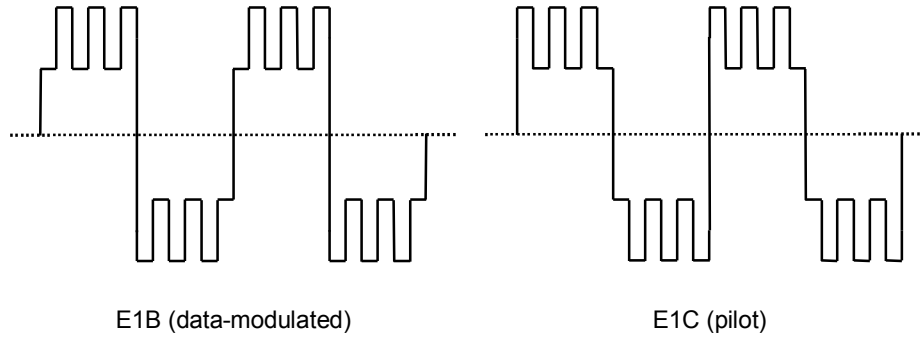


Figure G.3 CBOC subcarrier functions.

The MBOC design for the proposed Beidou B1-C signals was unknown at the time of writing.

G.3.2 Signal Multiplexing

Most GNSS signals form part of a multiplex of signals sharing a common carrier frequency. Signal multiplexes are commonly transmitted with in-phase and quadrature components to maximize transmission efficiency and minimize interference between the signal components. A multiplex of two BPSK signals has a total signal amplitude of

$$s(t) = \sqrt{2P_I} C_I(t) D_I(t) \cos(2\pi f_{ca} t + \phi_{ca}) + \sqrt{2P_Q} C_Q(t) D_Q(t) \sin(2\pi f_{ca} t + \phi_{ca}), \tag{G.2}$$

where the subscript I denotes the in-phase component and Q denotes the quadrature component. The combined signal multiplex has quadrature-phase shift key (QPSK) modulation. In the receiver, the in-phase component may be selected by multiplying by

$\cos(2\pi f_{ca}t + \phi_{ca})$ and the quadrature component by multiplying by $\sin(2\pi f_{ca}t + \phi_{ca})$ because the product $\cos(2\pi f_{ca}t + \phi_{ca})\sin(2\pi f_{ca}t + \phi_{ca})$ averages to zero over a carrier cycle.

Where there are two GNSS signals on a given frequency, a simple QPSK modulation is used with one signal broadcast on the in-phase component and the other on the quadrature component. Examples include GPS L1 from older satellites with only C/A-code and P(Y)-code signals, GPS L5, GLONASS L3, and all GLONASS FDMA signals.

For the Galileo E5a and E5b signals, a QPSK modulation is used on the individual carriers with the data components of the E5 signals, E5a-I and E5b-I, broadcast in-phase with respect to the carriers, while the pilot components, E5a-Q and E5b-Q, are broadcast in quadrature, i.e. 90° out of phase. However, this is not how they are transmitted. The Galileo satellites broadcast the E5a and E5b signals as a combined signal multiplex, enabling them to share a single transmitter. To enable the E5a-I and E5b-I signals to carry different navigation data messages, requiring differentiation of the sidebands, an alternate-binary-offset-carrier modulation scheme has been developed. This has a 15.345 MHz sub-carrier frequency and $10.23 \text{ Mchip s}^{-1}$ spreading code chipping rate.

Each of the four components of the AltBOC signal has a signal modulation with a constant phase with respect to the E5a or E5b carrier. Therefore the modulation phases with respect to the E5 AltBOC carrier rotate by one cycle per sub-carrier period, with the E5a and E5b components rotating in opposite directions. To combine these signals, the AltBOC sub-carrier modulation must perform the phase rotation. An eight-phase sub-carrier modulation is therefore applied which changes 8 times per sub-carrier period, as opposed to twice for conventional BOC modulation. The wideband signal comprises 8PSK modulation, as opposed to QPSK, enabling the receiver to separate the different signal modulations, E5a-I, E5b-I and the pilots. An intermodulation product term is added to maintain constant signal modulus for transmission efficiency; the receiver does not need to decode this [22–25].

Where three or more GNSS signals are combined on a single frequency, interplex modulation is used. An additional (non-useful) signal, comprising an intermodulation product of the other signals is often added to maintain a constant signal modulus. For the Galileo E1 and E6 signal multiplexes, each of which combine three useful signals, a tri-code hexaphase modulation is used [20, 26]. Note that this supersedes a coherent adaptive sub-carrier modulation (CASM) modulation proposed in some draft versions of the Galileo signal design.

Prior to transmission, the signals must be filtered to fit within the bandwidth listed in Table 8.4 in order to minimize adjacent band interference and comply with international law. To avoid significant signal distortion, the double-sided filtered bandwidth should be at least $2f_{co}$ for a BPSK signal, $2f_s + 2f_{co}$ for a sine-phased BOC signal, and $4f_s + 2f_{co}$ for a cosine-phased BOC signal. Consequently, the Galileo E1-A and E6-A signals are distorted, affecting ranging performance, particularly for the E1-A signal [27].

G.3.3 Ranging Code Design

Each GPS satellite transmits one of 36 C/A code sequences (originally 31), each allocated a PRN signal number and selected from a family of Gold codes to minimize cross-correlation [2, 28]. Each Gold code is $2n-1$ chips long, where n is an integer. It is obtained by the exclusive-or of two 1023-length codes, G1 and G2, with different offsets.

The GPS P code is a product of two PRN codes, known as X1 and X2, one of length 15,345,000 chips (1.5s) and the other 37 chips longer, giving a total code period of just over 38 weeks. Each GPS satellite transmits a different 1-week repeating segment of this code on both the L1 and L2 frequencies [2, 28].

The GPS L2C codes, CM and CL are linear patterns generated by a common code-generating 27^{th} order polynomial, but are truncated at different lengths (20ms and 1.5s, respectively). The CL-code epochs are aligned with the X1 code [28].

The primary GPS L5 codes are products of two PRN codes, XA and XB, of lengths 8,190 chips and 8,191 chips, respectively, each truncated at 10,230 chips (1ms). Different advances of the XB code are used for different satellites and for the I and Q components. The primary

codes are multiplied by 1 kchip s⁻¹ Neuman-Hofman codes to give full codes known as SpV codes [29].

The GPS L1C primary codes are Weil codes with a seven-bit expansion sequence inserted at some point. A Weil code comprises the exclusive-or of a length-10,223 Legendre sequence and a shifted version of the same sequence. The Legendre-sequence shift and expansion sequence insertion point are different for each satellite and for the data-modulated and pilot signals. The secondary codes for the pilot signals are derived from an 11th-order generator polynomial with a different coefficient for each signal [30].

The GLONASS C/A code is a 511-bit M-sequence generated by a shift register [31]. The L3 primary codes comprise a set of 16,383-chip Kasami sequences, each truncated at 10,230 chips (1 ms). The secondary codes are a 5-bit Barker code on the data-modulated signals and a 10-bit Neuman-Hofman code on the pilot signals [32].

Galileo open-service codes are memory codes, listed in the ICD [33]. All primary codes and the secondary codes for the E5a-Q and E5b-Q signals are unique to each satellite, while the secondary codes for the E5a-I, E5b-I, and E1-C signals are the same for all satellites.

G.4 Satellite Position, Velocity, and Acceleration

This section presents the satellite acceleration, building on the satellite position and velocity calculation in Section 8.5.2, the range acceleration, and the GLONASS satellite position and velocity calculation for use with the FDMA navigation message. The notation used in this section is defined in Sections 8.5.2 and 8.5.3.

G.4.1 Satellite and Range Acceleration

The range acceleration is useful for compensating data lags in the NCO control algorithms used in deeply coupled INS/GNSS integration (Section 14.3.3.5) and vector GNSS tracking (Section 10.3.7). Firstly, the satellite acceleration must be determined.

Differentiating (8.21) and (8.22) with respect to $t_{st,a}^s$ and applying (8.11),

$$\ddot{E} = -\frac{e_o \sin E}{1 - e_o \cos E} \dot{E}^2, \quad (\text{G.3})$$

$$\ddot{\Phi} = \frac{\sin v}{\sin E} \ddot{E} + \frac{\sin v (\cos v - \cos E)}{\sin^2 E} \dot{E}^2, \quad (\text{G.4})$$

Differentiating (8.23–8.26) gives, respectively,

$$\begin{aligned} \ddot{r}_{os}^o &= a e_o (\dot{E}^2 \cos E + \ddot{E} \sin E) + 2(C_{rs} \cos 2\Phi - C_{rc} \sin 2\Phi) \ddot{\Phi} - 4(C_{rs} \sin 2\Phi + C_{rc} \cos 2\Phi) \dot{\Phi}^2, \\ \ddot{u}_{os}^o &= (1 + 2C_{us} \cos 2\Phi - 2C_{uc} \sin 2\Phi) \ddot{\Phi} - 4(C_{us} \sin 2\Phi + C_{uc} \cos 2\Phi) \dot{\Phi}^2 \end{aligned} \quad (\text{G.5})$$

$$\begin{aligned} \ddot{x}_{os}^o &= \left(\ddot{r}_{os}^o - r_{os}^o \dot{u}_{os}^o{}^2 \right) \cos u_{os}^o - \left(2\dot{r}_{os}^o \dot{u}_{os}^o + r_{os}^o \ddot{u}_{os}^o \right) \sin u_{os}^o \\ \ddot{y}_{os}^o &= \left(\ddot{r}_{os}^o - r_{os}^o \dot{u}_{os}^o{}^2 \right) \sin u_{os}^o + \left(2\dot{r}_{os}^o \dot{u}_{os}^o + r_{os}^o \ddot{u}_{os}^o \right) \cos u_{os}^o, \\ \ddot{z}_{os}^o &= 0 \end{aligned} \quad (\text{G.6})$$

$$\ddot{\Omega} = \ddot{\Omega}_d = 0, \quad (\text{G.7})$$

$$\ddot{i} = 2(C_{is} \cos 2\Phi - C_{ic} \sin 2\Phi) \ddot{\Phi} - 4(C_{is} \sin 2\Phi + C_{ic} \cos 2\Phi) \dot{\Phi}^2, \quad (\text{G.8})$$

noting that \ddot{i}_d is zero.

Finally, differentiating (8.27) with respect to $t_{st,a}^s$ and substituting in (G.7) gives

$$\mathbf{a}_{es}^e = \begin{pmatrix} \ddot{x}_{os}^o \cos \Omega - [\ddot{y}_{os}^o \cos i - 2i\dot{y}_{os}^o \sin i - \ddot{y}_{os}^o \sin i - i^2 y_{os}^o \cos i] \sin \Omega \\ \ddot{x}_{os}^o \sin \Omega + [\ddot{y}_{os}^o \cos i - 2i\dot{y}_{os}^o \sin i - \ddot{y}_{os}^o \sin i - i^2 y_{os}^o \cos i] \cos \Omega \\ [\ddot{y}_{os}^o - i^2 y_{os}^o] \sin i + [2i\dot{y}_{os}^o + \ddot{y}_{os}^o] \cos i \end{pmatrix} \quad (G.9)$$

$$+ (\omega_{ie} - \dot{\Omega}_d) \begin{pmatrix} [2\dot{x}_{os}^o - \dot{\Omega} y_{os}^o \cos i] \sin \Omega + [\dot{x}_{os}^o \dot{\Omega} - 2i\dot{y}_{os}^o \sin i + 2\dot{y}_{os}^o \cos i] \cos \Omega \\ - [2\dot{x}_{os}^o - \dot{\Omega} y_{os}^o \cos i] \cos \Omega + [\dot{x}_{os}^o \dot{\Omega} - 2i\dot{y}_{os}^o \sin i + 2\dot{y}_{os}^o \cos i] \sin \Omega \\ 0 \end{pmatrix}$$

The ECI-frame acceleration is then determined by differentiating (8.28) with respect to $t_{st,a}^s$ and substituting in (G.7), giving

$$\mathbf{a}_{is}^i = \begin{pmatrix} \ddot{x}_{os}^o \cos [\Omega + \omega_{ie}(t_{st,a}^s - t_0)] - [\ddot{y}_{os}^o \cos i - 2i\dot{y}_{os}^o \sin i - \ddot{y}_{os}^o \sin i - i^2 y_{os}^o \cos i] \sin [\Omega + \omega_{ie}(t_{st,a}^s - t_0)] \\ \ddot{x}_{os}^o \sin [\Omega + \omega_{ie}(t_{st,a}^s - t_0)] + [\ddot{y}_{os}^o \cos i - 2i\dot{y}_{os}^o \sin i - \ddot{y}_{os}^o \sin i - i^2 y_{os}^o \cos i] \cos [\Omega + \omega_{ie}(t_{st,a}^s - t_0)] \\ [\ddot{y}_{os}^o - i^2 y_{os}^o] \sin i + [2i\dot{y}_{os}^o + \ddot{y}_{os}^o] \cos i \end{pmatrix}$$

$$+ \dot{\Omega}_d \begin{pmatrix} -2\dot{x}_{os}^o \sin [\Omega + \omega_{ie}(t_{st,a}^s - t_0)] + 2(\dot{y}_{os}^o \sin i - \dot{y}_{os}^o \cos i) \cos [\Omega + \omega_{ie}(t_{st,a}^s - t_0)] \\ 2\dot{x}_{os}^o \cos [\Omega + \omega_{ie}(t_{st,a}^s - t_0)] + 2(\dot{y}_{os}^o \sin i - \dot{y}_{os}^o \cos i) \sin [\Omega + \omega_{ie}(t_{st,a}^s - t_0)] \\ 0 \end{pmatrix}$$

$$- \dot{\Omega}_d^2 \begin{pmatrix} \dot{x}_{os}^o \cos [\Omega + \omega_{ie}(t_{st,a}^s - t_0)] - y_{os}^o \cos i \sin [\Omega + \omega_{ie}(t_{st,a}^s - t_0)] \\ \dot{x}_{os}^o \sin [\Omega + \omega_{ie}(t_{st,a}^s - t_0)] + y_{os}^o \cos i \cos [\Omega + \omega_{ie}(t_{st,a}^s - t_0)] \\ 0 \end{pmatrix} \quad (G.10)$$

The range acceleration is obtained by time-differentiating the range rate. From (8.42),

$$\ddot{r}_{as} = \frac{(\mathbf{r}_{is}^i(t_{st,a}^s) - \mathbf{r}_{ia}^i(t_{sa,a}^s))^T (\ddot{\mathbf{r}}_{is}^i(t_{st,a}^s) - \ddot{\mathbf{r}}_{ia}^i(t_{sa,a}^s))}{r_{as}} + \frac{(\dot{\mathbf{r}}_{is}^i(t_{st,a}^s) - \dot{\mathbf{r}}_{ia}^i(t_{sa,a}^s))^T (\dot{\mathbf{r}}_{is}^i(t_{st,a}^s) - \dot{\mathbf{r}}_{ia}^i(t_{sa,a}^s))}{r_{as}}$$

$$- \frac{\dot{r}_{as} (\mathbf{r}_{is}^i(t_{st,a}^s) - \mathbf{r}_{ia}^i(t_{sa,a}^s))^T (\dot{\mathbf{r}}_{is}^i(t_{st,a}^s) - \dot{\mathbf{r}}_{ia}^i(t_{sa,a}^s))}{r_{as}^2} \quad (G.11)$$

Substituting in (8.30), (8.40), and (8.43),

$$\ddot{r}_{as} = \mathbf{u}_{as}^i{}^T (\mathbf{a}_{is}^i(t_{st,a}^s) - \mathbf{a}_{ia}^i(t_{sa,a}^s))$$

$$+ \left([\mathbf{v}_{is}^i(t_{st,a}^s) - \mathbf{v}_{ia}^i(t_{sa,a}^s)] - \frac{\mathbf{u}_{as}^i{}^T [\mathbf{v}_{is}^i(t_{st,a}^s) - \mathbf{v}_{ia}^i(t_{sa,a}^s)]}{|\mathbf{r}_{is}^i(t_{st,a}^s) - \mathbf{r}_{ia}^i(t_{sa,a}^s)|} [\mathbf{r}_{is}^i(t_{st,a}^s) - \mathbf{r}_{ia}^i(t_{sa,a}^s)] \right)^T \frac{[\mathbf{v}_{is}^i(t_{st,a}^s) - \mathbf{v}_{ia}^i(t_{sa,a}^s)]}{|\mathbf{r}_{is}^i(t_{st,a}^s) - \mathbf{r}_{ia}^i(t_{sa,a}^s)|} \quad (G.12)$$

From (2.145–2.148), this may be expressed in terms of ECEF-frame positions, velocities, and accelerations as follows:

$$\begin{aligned}
\ddot{\mathbf{r}}_{as}^e &= \mathbf{u}_{as}^{eT} \left[\mathbf{C}_e^I(t_{st,a}^s) (\mathbf{a}_{es}^e(t_{st,a}^s) + 2\mathbf{\Omega}_{ie}^e \mathbf{v}_{es}^e(t_{st,a}^s) + \mathbf{\Omega}_{ie}^e \mathbf{\Omega}_{ie}^e \mathbf{r}_{es}^e(t_{st,a}^s)) \right. \\
&\quad \left. - (\mathbf{a}_{ea}^e(t_{sa,a}^s) + 2\mathbf{\Omega}_{ie}^e \mathbf{v}_{ea}^e(t_{sa,a}^s) + \mathbf{\Omega}_{ie}^e \mathbf{\Omega}_{ie}^e \mathbf{r}_{ea}^e(t_{sa,a}^s)) \right] \\
&\quad + \mathbf{v}_{as}'^T \left[\frac{\mathbf{C}_e^I(t_{st,a}^s) (\mathbf{v}_{es}^e(t_{st,a}^s) + \mathbf{\Omega}_{ie}^e \mathbf{r}_{es}^e(t_{st,a}^s)) - (\mathbf{v}_{ea}^e(t_{sa,a}^s) + \mathbf{\Omega}_{ie}^e \mathbf{r}_{ea}^e(t_{sa,a}^s))}{\left| \mathbf{C}_e^I(t_{st,a}^s) \mathbf{r}_{es}^e(t_{st,a}^s) - \mathbf{r}_{ea}^e(t_{sa,a}^s) \right|}} \right] \\
\mathbf{v}_{as}' &= \left[\mathbf{C}_e^I(t_{st,a}^s) (\mathbf{v}_{es}^e(t_{st,a}^s) + \mathbf{\Omega}_{ie}^e \mathbf{r}_{es}^e(t_{st,a}^s)) - (\mathbf{v}_{ea}^e(t_{sa,a}^s) + \mathbf{\Omega}_{ie}^e \mathbf{r}_{ea}^e(t_{sa,a}^s)) \right] \\
&\quad - \left[\frac{\mathbf{u}_{as}^{eT} \left[\mathbf{C}_e^I(t_{st,a}^s) (\mathbf{v}_{es}^e(t_{st,a}^s) + \mathbf{\Omega}_{ie}^e \mathbf{r}_{es}^e(t_{st,a}^s)) - (\mathbf{v}_{ea}^e(t_{sa,a}^s) + \mathbf{\Omega}_{ie}^e \mathbf{r}_{ea}^e(t_{sa,a}^s)) \right]}{\left| \mathbf{C}_e^I(t_{st,a}^s) \mathbf{r}_{es}^e(t_{st,a}^s) - \mathbf{r}_{ea}^e(t_{sa,a}^s) \right|}} \right] \\
&\quad \times \left[\mathbf{C}_e^I(t_{st,a}^s) \mathbf{r}_{es}^e(t_{st,a}^s) - \mathbf{r}_{ea}^e(t_{sa,a}^s) \right]
\end{aligned} \quad (G.13)$$

For deeply coupled INS/GNSS integration, the user antenna acceleration may be obtained from the inertial acceleration using (2.166):

$$\hat{\mathbf{a}}_{\beta a}^{\gamma} \approx \hat{\mathbf{a}}_{\beta b}^{\gamma} + \hat{\mathbf{C}}_b^{\gamma} \left[\hat{\boldsymbol{\omega}}_{ib}^b \wedge (\hat{\boldsymbol{\omega}}_{ib}^b \wedge \mathbf{l}_{ba}^b) + (\hat{\boldsymbol{\omega}}_{ib}^b \wedge \mathbf{l}_{ba}^b) \right], \quad \{\beta, \gamma\} \in \{i, i\}, \{e, e\}, \{e, n\}, \quad (G.14)$$

where the effect of Earth rotation on the lever arm acceleration has been neglected.

G.4.2 GLONASS Satellite Position and Velocity Calculation

In the GLONASS FDMA navigation messages, satellite position is expressed in terms of the ECEF-frame position and velocity at the reference time, t_{oe} , together with the lunisolar acceleration, \mathbf{a}_{LS}^e . The ECEF-frame acceleration is then obtained by applying a gravity model, giving [34]

$$\mathbf{a}_{es}^e = -\frac{\mu}{|\mathbf{r}_{es}^e|^3} \left\{ \mathbf{r}_{es}^e + \frac{3}{2} J_2 \frac{R_0^2}{|\mathbf{r}_{es}^e|^2} \begin{bmatrix} \left[1 - 5 \left(\frac{z_{es}^e}{|\mathbf{r}_{es}^e|} \right)^2 \right] x_{es}^e \\ \left[1 - 5 \left(\frac{z_{es}^e}{|\mathbf{r}_{es}^e|} \right)^2 \right] y_{es}^e \\ \left[3 - 5 \left(\frac{z_{es}^e}{|\mathbf{r}_{es}^e|} \right)^2 \right] z_{es}^e \end{bmatrix} \right\} + \begin{pmatrix} \omega_{ie}^2 x_{es}^e + 2\omega_{ie} v_{es,y}^e \\ \omega_{ie}^2 y_{es}^e - 2\omega_{ie} v_{es,x}^e \\ 0 \end{pmatrix} + \mathbf{a}_{LS}^e. \quad (G.15)$$

Fourth-order Runge-Kutta numerical integration may then be used to determine the satellite position and velocity at the time of interest from their counterparts at t_{oe} . This proceeds iteratively with position and velocity calculated at a number of intermediate times until the desired time is reached. Time steps of between 1 and 30 seconds may be used, depending on the precision required. For propagation over a time interval, τ , which may be positive or negative, the following steps are performed [34]:

$$\begin{aligned}
\mathbf{k}_{v1} &= \mathbf{a}_{es}^e(\mathbf{r}_{es}^e(t), \mathbf{v}_{es}^e(t)) \tau & \mathbf{k}_{r1} &= \mathbf{v}_{es}^e(t) \tau \\
\mathbf{k}_{v2} &= \mathbf{a}_{es}^e \left(\mathbf{r}_{es}^e(t) + \frac{1}{2} \mathbf{k}_{r1}, \left[\mathbf{v}_{es}^e(t) + \frac{1}{2} \mathbf{k}_{v1} \right] \right) \tau & \mathbf{k}_{r2} &= \left[\mathbf{v}_{es}^e(t) + \frac{1}{2} \mathbf{k}_{v1} \right] \tau \\
\mathbf{k}_{v3} &= \mathbf{a}_{es}^e \left(\mathbf{r}_{es}^e(t) + \frac{1}{2} \mathbf{k}_{r2}, \left[\mathbf{v}_{es}^e(t) + \frac{1}{2} \mathbf{k}_{v2} \right] \right) \tau & \mathbf{k}_{r3} &= \left[\mathbf{v}_{es}^e(t) + \frac{1}{2} \mathbf{k}_{v2} \right] \tau \\
\mathbf{k}_{v4} &= \mathbf{a}_{es}^e \left(\mathbf{r}_{es}^e(t) + \mathbf{k}_{r3}, \left[\mathbf{v}_{es}^e(t) + \mathbf{k}_{v3} \right] \right) \tau & \mathbf{k}_{r4} &= \left[\mathbf{v}_{es}^e(t) + \mathbf{k}_{v3} \right] \tau \\
\mathbf{v}_{es}^e(t + \tau) &= \mathbf{v}_{es}^e(t) + \frac{1}{6} (\mathbf{k}_{v1} + 2\mathbf{k}_{v2} + 2\mathbf{k}_{v3} + \mathbf{k}_{v4}) \tau \\
\mathbf{r}_{es}^e(t + \tau) &= \mathbf{r}_{es}^e(t) + \frac{1}{6} (\mathbf{k}_{r1} + 2\mathbf{k}_{r2} + 2\mathbf{k}_{r3} + \mathbf{k}_{r4}) \tau
\end{aligned} \quad (G.16)$$

The satellite position and velocity may be transformed to the ECI frame using (2.145–2.147).

G.5 Relativistic Frequency Shift

The received frequency of a radio signal differs from the transmitted frequency due to the classical Doppler shift and to time dilation arising from both special and general relativity [35]. The relativistic effects may generally be neglected for terrestrial radio navigation. However, for GNSS, they are significant. For all receivers located on the geoid (Section 2.4.4) and stationary with respect to the Earth, the total time dilation is the same (though the balance between special and general relativistic effects varies). A frequency shift is applied to the transmitted signal that cancels out the average relativistic frequency shift for these receivers.

For high-velocity and high-precision applications, further corrections must be applied within the user equipment to account for variations in the satellite time dilation due to the elliptical orbit, the motion of the user antenna with respect to the Earth, and the distance of the user antenna from the geoid. In this case, the pseudo-range rate, $\tilde{\rho}_{a,R}^{s,l}$, is obtained from the frequency shift (from the nominal carrier frequency), $\Delta f_{ca,a}^s$, using [35, 36]

$$\tilde{\rho}_{a,R}^{s,l} \approx -\frac{c}{f_{ca}} \Delta f_{ca,a}^{s,l} + \delta \hat{\rho}_r^a - \delta \hat{\rho}_r^s, \quad (\text{G.17})$$

where $\delta \hat{\rho}_r^a$ and $\delta \hat{\rho}_r^s$ are the estimated range rate errors due to residual relativistic time dilation at the user antenna and satellite, respectively. These are given by

$$\begin{aligned} \delta \hat{\rho}_r^a \approx & -\frac{1}{2c} \left(\frac{\omega_{ie}^2 \cos^2 L_a [2R_E(L_a)h_a + h_a^2] + (v_{ea,E}^n)^2 + 2v_{ea,E}^n \omega_{ie} [R_E(L_a) + h_a] \cos L_a}{[R_N(L_a) + h_a]^2} \left\{ [R_E(L_a) + h_a]^2 + e^2 R_E(L_a) [(e^2 - 2)R_E(L_a) - 2h_a] \sin^2 L_a \right\} \right. \\ & - \frac{1}{2c} \left(\frac{(v_{ea,N}^n)^2}{[R_N(L_a) + h_a]^2} \left\{ e^4 R_N^2(L_a) \sin^6 L_a + \cos^2 L_a [R_N(L_a) - R_E(L_a)]^2 \right\} \right. \\ & \left. \left. + (v_{ea,D}^n)^2 + 2e^2 v_{ea,N}^n v_{ea,D}^n \frac{R_E(L_a) + h_a}{R_N(L_a) + h_a} \sin L_a \cos L_a \right. \right. \\ & \left. \left. - \frac{g_0(L_a)H_a}{c} \right) \right) \end{aligned} \quad (\text{G.18})$$

and

$$\delta \hat{\rho}_r^s = -\frac{2}{c} \left(\mathbf{v}_{es}^e \mathbf{v}_{es}^e + \mathbf{r}_{es}^e \mathbf{a}_{es}^e \right), \quad (\text{G.19})$$

where the notation is as defined in Chapter 2, the satellite position and velocity are given in Section 8.5.2, and the satellite acceleration is given in Section G.4.1.

G.6 Receiver and Ranging Processor Design Notes

This section presents some additional notes on postcorrelation signal to noise, BOC signal tracking, and C/N_0 measurement. The notation used in this section is defined in Section 9.1.

G.6.1 Postcorrelation Signal to Noise

From (9.6), (9.7), and (9.9), the postcorrelation signal amplitude is simply

$$A_C = f_a \tau_a A_0, \quad (\text{G.20})$$

while the postcorrelation noise standard deviation is

$$\sigma_{IQ} = f_a \sqrt{E \left\{ \left[\int_{t_{sa}-\tau_a}^{t_{sa}} w_{I0}(t) C(t + \tilde{t}_{st} - t_{sa}) dt \right]^2 \right\}}, \quad (G.21)$$

where E is the expectation operator. Averaging the noise samples, $w_{I0}(t)$, over each code chip to give samples, $w_{Ico,i}$, indexed by chip,

$$\sigma_{IQ}^2 = \frac{f_a^2}{f_{co}^2} \sum_{i=i_0}^{i_0+f_{co}\tau_a-1} \sum_{j=i_0}^{i_0+f_{co}\tau_a-1} E(w_{Ico,i} C_i w_{Ico,j} C_j), \quad (G.22)$$

noting that, in practice, the number of samples per chip is not an integer. As successive code chips are uncorrelated, $E(C_i C_j) = \delta_{ij}$, so

$$\sigma_{IQ}^2 = \frac{f_a^2}{f_{co}^2} \tau_a E(w_{Ico}^2). \quad (G.23)$$

If the noise is white with single-sided power spectral density n_0 , then, from (B.114), the variance of the noise averaged over one code chip is $n_0 f_{co}$, provided that the double-sided pre-correlation bandwidth, B_{PC} , is at least twice the chipping rate, f_{co} . From (9.6) and (9.1), the signal and noise amplitudes are boosted through the receiver front-end and AGC by a factor of $A_0/\sqrt{2P}$. Therefore

$$E(w_{Ico}^2) = \frac{A_0^2 n_0 f_{co}}{2P}, \quad (G.24)$$

and

$$\sigma_{IQ} = A_0 f_a \sqrt{\frac{n_0 \tau_a}{2P}}. \quad (G.25)$$

Where the noise is not white, the PSD should be weighted by the GNSS signal spectrum using

$$n_0 = 2 \frac{\int_{-\infty}^{\infty} S_w^f(f) S_s^f(f) df}{\int_{-\infty}^{\infty} S_s^f(f) df}. \quad (G.26)$$

where S_w^f is the double-sided noise PSD and S_s^f is the double-sided signal PSD (the factor of 2 converts from double-sided to single-sided).

The ratio of the received signal power, P , to the weighted noise PSD, n_0 , is known as the carrier power to noise density, c/n_0 (see Section 9.1.4.2). Thus, from, (G.20) and (G.25), the postcorrelation signal to noise amplitude ratio is

$$\frac{A_c}{\sigma_{IQ}} = \sqrt{2(c/n_0)\tau_a}, \quad (G.27)$$

while the postcorrelation power ratio is

$$\frac{P_c}{\sigma_{IQ}^2} = \frac{\frac{1}{2} A_c^2}{\sigma_{IQ}^2} = (c/n_0)\tau_a, \quad (G.28)$$

G.6.2 BOC Tracking

As shown in Section 9.2.2, BOC signal tracking using techniques for BPSK signals is inherently ambiguous with a risk of the code tracking loop locking onto a minor peak of the correlation function (Figure 9.7). To resolve this, bespoke BOC tracking techniques are

required. This section presents more details of the double-estimator and bump-jumping techniques and summarizes some other methods.

A double estimator [37–40] may be implemented using six correlators per signal. The accumulated correlator outputs are given by

$$\begin{aligned} I_P(t_{sa}) &= f_a \int_{t_{sa}-\tau_a}^{t_{sa}} I_0(t) C_P(t) S_P(t) dt, & Q_P(t_{sa}) &= f_a \int_{t_{sa}-\tau_a}^{t_{sa}} Q_0(t) C_P(t) S_P(t) dt \\ I_{P\Delta}(t_{sa}) &= f_a \int_{t_{sa}-\tau_a}^{t_{sa}} I_0(t) C_P(t) S_\Delta(t) dt, & Q_{P\Delta}(t_{sa}) &= f_a \int_{t_{sa}-\tau_a}^{t_{sa}} Q_0(t) C_P(t) S_\Delta(t) dt \\ I_{E-L}(t_{sa}) &= f_a \int_{t_{sa}-\tau_a}^{t_{sa}} I_0(t) C_{E-L}(t) S_P(t) dt, & Q_{E-L}(t_{sa}) &= f_a \int_{t_{sa}-\tau_a}^{t_{sa}} Q_0(t) C_{E-L}(t) S_P(t) dt \end{aligned} \quad (G.29)$$

where I_0 and Q_0 are given by (9.16), C_P is given by (9.7), C_{E-L} is given by (9.8), S_P is given by (9.18), and S_Δ is given by (9.21).

A conventional code tracking loop is implemented, as described in Section 9.2.2. Suitable discriminators include the DPP and decision-directed coherent discriminators, given by:

$$\begin{aligned} D_{DPP} &= I_{E-L} I_P + Q_{E-L} Q_P \\ D_{Coh} &= I_{E-L} \text{sign}(I_P) \end{aligned} \quad (G.30)$$

These are insensitive to the subcarrier phase.

An additional subcarrier tracking loop is also implemented. This has the same design as a code tracking loop except that the discriminator is sensitive to the subcarrier phase and insensitive to the PRN-code phase. Suitable discriminators include

$$\begin{aligned} S_{DPP} &= I_{P\Delta} I_P + Q_{P\Delta} Q_P \\ S_{Coh} &= I_{P\Delta} \text{sign}(I_P) \end{aligned} \quad (G.31)$$

The double estimator code-phase estimate, \tilde{t}'_{st} , may be obtained from the PRN code-phase estimate, $\tilde{t}'_{st,C}$, and subcarrier-derived code phase estimate, $\tilde{t}'_{st,S}$, using

$$\tilde{t}'_{st} = \tilde{t}'_{st,S} + \frac{\text{round}[(\tilde{t}'_{st,C} - \tilde{t}'_{st,S})f_s]}{f_s}, \quad (G.32)$$

where the ‘round’ function rounds its argument to the nearest integer. Thus, the PRN code-phase estimate is used to resolve the ambiguity in the subcarrier-derived code phase estimate.

A *triple estimator* [41] has also been designed for tracking MBOC signals. This implements separate subcarrier tracking loops for the 1.023-MHz and 6.138-MHz subcarriers.

Bump jumping uses conventional correlation and code tracking to track the central peak of the correlation function [42]. Thus, the accumulated correlator outputs given by (9.17) are used with the early-late correlator spacing, d , typically set to $f_{co} / 4f_s$. Additional very early (VE) and very late (VL) correlators are then implemented at offsets of half a subcarrier period from the prompt correlators as illustrated for a BOC_s(10,5) signal in Figure G.4. Thus,

$$\begin{aligned} I_{VE}(t_{sa}) &= f_a \int_{t_{sa}-\tau_a}^{t_{sa}} I_0(t) C_{VE}(t) S_{VE}(t) dt, & Q_{VE}(t_{sa}) &= f_a \int_{t_{sa}-\tau_a}^{t_{sa}} Q_0(t) C_{VE}(t) S_{VE}(t) dt \\ I_{VL}(t_{sa}) &= f_a \int_{t_{sa}-\tau_a}^{t_{sa}} I_0(t) C_{VL}(t) S_{VL}(t) dt, & Q_{VL}(t_{sa}) &= f_a \int_{t_{sa}-\tau_a}^{t_{sa}} Q_0(t) C_{VL}(t) S_{VL}(t) dt \end{aligned} \quad (G.33)$$

where

$$\begin{aligned}
C_{VE}(t_{sa}) &= C(\tilde{t}_{st} + 1/2f_s), & S_{VE}(t_{sa}) &= S(\tilde{t}_{st} + 1/2f_s) \\
C_{VL}(t_{sa}) &= C(\tilde{t}_{st} - 1/2f_s), & S_{VL}(t_{sa}) &= S(\tilde{t}_{st} - 1/2f_s)
\end{aligned}
\tag{G.34}$$

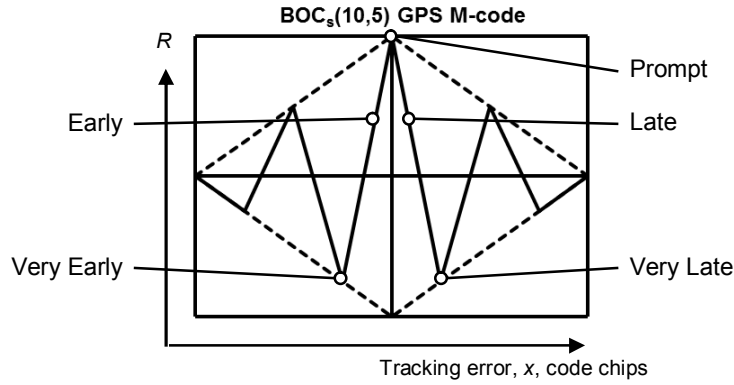


Figure G.4 Correlator positions for BOC_s(10,5) code tracking using bump jumping.

The bump jumping algorithm maintains early and late counters, respectively, c_E and c_L using

$$\begin{aligned}
I_{VE}^2 + Q_{VE}^2 &> I_P^2 + Q_P^2 && \Rightarrow c_E := c_E + 1 \\
(I_{VE}^2 + Q_{VE}^2 \leq I_P^2 + Q_P^2) \text{ AND } (c_E > 0) && \Rightarrow c_E := c_E - 1
\end{aligned}
\tag{G.35}$$

and

$$\begin{aligned}
I_{VL}^2 + Q_{VL}^2 &> I_P^2 + Q_P^2 && \Rightarrow c_L := c_L + 1 \\
(I_{VL}^2 + Q_{VL}^2 \leq I_P^2 + Q_P^2) \text{ AND } (c_L > 0) && \Rightarrow c_L := c_L - 1
\end{aligned}
\tag{G.36}$$

If c_E reaches the bump-jumping threshold, the code-phase estimate, \tilde{t}_{st}' , is advanced by half a sub-carrier period, $1/2f_s$, and both counters are reset. Similarly, if c_L reaches the bump-jumping threshold, \tilde{t}_{st}' , is retarded by $1/2f_s$, and the counters reset.

The multiple-gate discriminator (MGD) method uses an array of correlator pairs, all of which contribute to the code discriminator function. The spacing of the correlator pairs and their weighting in the discriminator are adjusted to produce an unambiguous discriminator function similar to those shown in Figure 9.13 [37, 43]. The number of correlators required is $4f_s / f_{co}$, so the technique is more costly to implement for BOC modulations with higher subcarrier to chipping rate ratios.

A number of techniques are designed for specific subcarrier to chipping rate ratios. Signals for which $f_s = f_{co}$, such as BOC_s(1,1), may be correlated with the equivalent prompt BPSK code in place of the early and late correlation channels, giving a cross-correlation function which may be used as the code discriminator [44].

The autocorrelation side-peak cancellation technique (ASPECT) is also designed for signals with $f_s = f_{co}$. The early, prompt, and late correlation channels are duplicated with one set correlating the signal with a BOC reference signal and the other with the corresponding BPSK code. The accumulated correlator outputs are then combined at the code discriminator [45].

Signals with $f_s = 2f_{co}$ may be correlated with two reference signals, each with differently modified subcarrier symbols. Again, the accumulated correlator outputs are combined at the code discriminator [46].

Finally, the simplest technique is to track a single sidelobe as a BPSK signal. However, half the signal power is lost and the precision is significantly degraded. Even if both sidelobes are independently correlated and combined noncoherently at the discriminator (which requires dual front-ends), the precision is degraded by a factor of $4f_s / f_{co}$ compared to the preceding techniques [37].

Note that bandlimiting of the $\text{BOC}_c(15,2.5)$ -modulated Galileo E1-A renders the central peak of the correlation function only 3.5% larger than the adjacent peaks. This can make it difficult to identify the correct peak, particularly in a low signal-to-noise environment. Furthermore, multipath interference can distort the correlation function such that the central peak is no longer the largest [27]. Therefore, noncoherent tracking may give better performance.

G.6.3 Carrier-Power-to-Noise-Density Measurement

This section presents some alternative c/n_0 measurement methods to the narrow-to-wide power-ratio method described in Section 9.2.6. An adaptation of the narrow-to-wide power-ratio method to use early or late discriminator outputs instead of prompt is presented in [47].

In principle, c/n_0 may be estimated either before or after the signal is correlated with the reference code. However, precorrelation signal-to-noise measurement techniques are affected by the noise spectrum. They overestimate c/n_0 where the interference is concentrated near the center of the signal spectrum and underestimate it where the interference is concentrated away from the main signal peak [48, 49]. Therefore, only postcorrelation techniques are considered here.

The correlator-comparison method compares the narrowband power with the output, I_N , of a noise correlation channel, which correlates the incoming signal with an unused PRN code. The measurement averaged over n iterations is [50]

$$Z_{cc} = \sum_{k=1}^n (I_{P,k}^2 + Q_{P,k}^2) / \sum_{k=1}^n I_{N,k}^2, \quad (\text{G.37})$$

where $I_{P,k}$, $Q_{P,k}$, and $I_{N,k}$ are accumulated over time τ_a . Taking expectations,

$$E(Z_{cc}) \approx [(c/n_0)\tau_a + 1] \left(1 + \frac{2}{n}\right), \quad (\text{G.38})$$

giving

$$\tilde{c}/\tilde{n}_0 = \frac{1}{\tau_a} \left(\frac{n}{n+2} Z_{cc} - 1 \right). \quad (\text{G.39})$$

Performance is similar to the narrow-to-wide power-ratio method.

The moments method uses the second- and fourth-order moments of the correlator outputs to separately estimate the carrier and noise strength [51]. The moments are

$$Z_2 = \frac{1}{n} \sum_{k=1}^n (I_{P,k}^2 + Q_{P,k}^2), \quad Z_4 = \frac{1}{n} \sum_{k=1}^n (I_{P,k}^2 + Q_{P,k}^2)^2 \quad (\text{G.40})$$

and the estimated carrier power to noise density is

$$\tilde{c}/\tilde{n}_0 = \frac{\sqrt{2Z_2^2 - Z_4}}{(Z_2 - \sqrt{2Z_2^2 - Z_4})\tau_a}. \quad (\text{G.41})$$

This method has the advantage over the narrow-to-wide power-ratio method of producing unbiased measurements at large values of C/N_0 , over 50 dB-Hz. However, at lower C/N_0 , it is noisier [51].

A discriminator-statistics method may also be used [50] and there are further methods that rely on carrier-phase lock [51]. Finally, where separate navigation-data-modulated and pilot signals are broadcast on the same frequency, c/n_0 may be estimated by comparing the two signals [52].

G.7 Range Error Corrections

This section presents additional information (to Section 9.3) on correcting GNSS range errors. Intersignal timing biases; the Klobuchar and SBAS ionosphere models; and the NATO, WAAS, and UNB3 troposphere models are described.

G.7.1 Intersignal Timing Biases

The intersignal timing bias terms within the satellite clock corrections (see Section 9.3.1) may be treated as constants and are very similar for signals of the same design. They are calculated using information transmitted in the navigation data messages. For GPS [28, 53],

$$\begin{aligned}\Delta a_{is}^{s,L1P(Y)} &= -T_{GD}^s \\ \Delta a_{is}^{s,L2P(Y)} &= -\left(f_{ca}^{L1} / f_{ca}^{L2}\right)^2 T_{GD}^s \\ \Delta a_{is}^{s,l} &= ISC_l^s - T_{GD}^s, \quad l \in C/A, L1C-d, L1C-p, L2C, L5I, L5Q\end{aligned}\quad (G.42)$$

where T_{GD}^s is the group delay correction and ISC_l^s are the intersignal corrections. Note that intersignal corrections are only transmitted in the newer messages, so users of legacy equipment must assume that the C/A code is synchronized with the L1 P(Y) code.

For the GLONASS FDMA signals, no information is provided in the navigation message for calculating intersignal biases. However, the satellites are designed so that all signals are synchronized to the reference oscillator to within 2 ns (0.6m) [41].

For Galileo, two separate sets of clock calibration coefficients (see Section 9.3.1), together with a broadcast group delay, B_{GD}^s , are broadcast for the (E1, E5a) and (E1, E5b) signal combinations [33]. Denoting these with the subscripts a and b , the intersignal timing biases are then

$$\begin{aligned}\Delta a_{is,a}^{s,E1} &= -B_{GD,a}^s & \Delta a_{is,b}^{s,E1} &= -B_{GD,b}^s \\ \Delta a_{is,a}^{s,E5a} &= -\left(f_{ca}^{E1} / f_{ca}^{E5a}\right)^2 B_{GD,a}^s & \Delta a_{is,b}^{s,E5b} &= -\left(f_{ca}^{E1} / f_{ca}^{E5b}\right)^2 B_{GD,b}^s\end{aligned}\quad (G.43)$$

noting that different Galileo signals transmitted on the same frequency are assumed to be synchronized.

For linear combinations of pseudo-range or ADR measurements, the corresponding linear combination of the intersignal timing bias must be used to determine the satellite clock corrections. Thus for the ionosphere-corrected pseudo-range, given by (9.82), the intersignal timing bias is given by

$$\Delta a_{is}^{s,ic} = \frac{\left(f_{ca}^\alpha\right)^2 \Delta a_{is}^{s,\alpha} - \left(f_{ca}^\beta\right)^2 \Delta a_{is}^{s,\beta}}{\left(f_{ca}^\alpha\right)^2 - \left(f_{ca}^\beta\right)^2}, \quad (G.44)$$

where $\Delta a_{is}^{s,\alpha}$ and $\Delta a_{is}^{s,\beta}$ are the intersignal timing biases of signals α and β , respectively. This also applies to the smoothed ionosphere-corrected pseudo-ranges, given by (9.84), (9.86) and (9.89). From (G.42–44), the ionosphere-corrected intersignal timing bias is zero for the combinations GPS L1 P(Y) and L2 P(Y), Galileo E1 and E5a, and Galileo E1 and E5b.

G.7.2 Klobuchar Ionosphere Model

In a single-frequency GNSS receiver, the ionosphere propagation delay, $\delta\rho_{I,a}^{s,l}$, is often estimated using the Klobuchar model, [28, 53]. This calculates the delay as a function of the antenna latitude and longitude, L_a and λ_a ; the satellite elevation and azimuth, θ_{nu}^{as} and ψ_{nu}^{as} ; the time; and the coefficients, $\alpha_0, \alpha_1, \alpha_2, \alpha_3, \beta_0, \beta_1, \beta_2$, and β_3 transmitted in the GPS navigation data message. Note that constants are radian-based here, whereas semicircles are used in [28, 53].

The first steps are to determine the Earth-centered angle, Ψ_E^s , and the subionospheric latitude, L_I^s :

$$\Psi_E^s = \frac{0.1352}{\theta_{nu}^{as} + 0.3456} - 0.06912 \text{ rad}, \quad (\text{G.45})$$

$$L_I^s = L_a + \Psi_E^s \cos \psi_{nu}^{as}. \quad (\text{G.46})$$

The subionospheric latitude is then limited to the range $-1.307 \leq L_I^s \leq 1.307$ rad and used to calculate the subionospheric longitude, λ_I^s , and geomagnetic latitude, L_m^s :

$$\lambda_I^s = \lambda_a + \Psi_E^s \frac{\sin \psi_{nu}^{as}}{\cos L_I^s}, \quad (\text{G.47})$$

$$L_m^s = L_I^s + 0.201 \cos(\lambda_I^s - 5.080) \text{ rad}. \quad (\text{G.48})$$

Finally, the time at the subionospheric point, t_{si}^s , is calculated:

$$t_{si}^s = \Delta t'^s + 1.375 \times 10^4 \lambda_I^s \text{ s}, \quad (\text{G.49})$$

where $\Delta t'^s$ is obtained by limiting Δt^s (calculated in Section 8.5.2) to the range $0 \leq \Delta t'^s \leq 86,400$ s by adding or subtracting integer multiples of 86,400 s.

The estimated ionosphere propagation delay for a signal in the GPS L1 band is then

$$\begin{aligned} \delta \hat{\rho}_{I,a}^{s,L1} = & \begin{cases} 5 \times 10^{-9} \left(1.0 + 0.516 \left(1.67 - \theta_{nu}^{as} \right)^3 \right) \text{ s} & |x_s| > 1.57 \\ \left(5 \times 10^{-9} + \left(1 - \frac{x_s^2}{2} + \frac{x_s^4}{24} \right) \sum_{n=0}^3 \alpha_n \left(\frac{L_m^s}{\pi} \right)^n \right) \left(1.0 + 0.516 \left(1.67 - \theta_{nu}^{as} \right)^3 \right) \text{ s} & |x_s| \leq 1.57 \end{cases} \end{aligned} \quad (\text{G.50})$$

where

$$x_s = \frac{2\pi(t_{si}^s - 50,400 \text{ s})}{\sum_{n=0}^3 \beta_n (L_m^s / \pi)^n}. \quad (\text{G.51})$$

The estimated delay for a generic signal, l , is then

$$\delta \hat{\rho}_{I,a}^{s,l} = \left(\frac{f_{ca}^{L1}}{f_{ca}^l} \right)^2 \delta \hat{\rho}_{I,a}^{s,L1}. \quad (\text{G.52})$$

G.7.3 SBAS Ionosphere Model

SBAS satellites transmit the total electron count (TEC) for signals passing vertically through the atmosphere at a grid of pierce points. The pierce point of the signal from satellite s is located at the subionospheric latitude and longitude, L_I^s and λ_I^s , calculated as described in the preceding section. The vertical TEC at this point, T_V^s , is obtained from the four nearest grid points by interpolation:

$$T_V^s = \left| \frac{L_I^s - L_j}{L_j - L_i} \right| \left(\left| \frac{\lambda_I^s - \lambda_j}{\lambda_j - \lambda_i} \right| T_V(L_i, \lambda_i) + \left| \frac{\lambda_I^s - \lambda_i}{\lambda_j - \lambda_i} \right| T_V(L_i, \lambda_j) \right) + \left| \frac{L_I^s - L_i}{L_j - L_i} \right| \left(\left| \frac{\lambda_I^s - \lambda_j}{\lambda_j - \lambda_i} \right| T_V(L_j, \lambda_i) + \left| \frac{\lambda_I^s - \lambda_i}{\lambda_j - \lambda_i} \right| T_V(L_j, \lambda_j) \right) \quad (G.53)$$

The estimated ionospheric delay for a generic signal is then [55]

$$\delta \hat{\rho}_{I,a}^{s,l} = \frac{40.3 T_V}{(f_{ca}^j)^2 \sqrt{1 - 0.8985 \cos^2 \theta_{nu}^{as}}} \quad (G.54)$$

G.7.4 WAAS Troposphere Delay Model

The troposphere propagation delay estimated by the initial WAAS model is [56]

$$\delta \hat{\rho}_{T,a}^s = \frac{2.506 \left(1 + 1.25 \times 10^{-3} \delta N_s \right)}{\sin(\theta_{nu}^{as} + 6.11 \times 10^{-3} \text{ rad})} (1 - 1.264 \times 10^{-4} H_a) \text{ m}, \quad (G.55)$$

for $H_a \leq 1,500\text{m}$ and

$$\delta \hat{\rho}_{T,a}^s = \frac{2.484 \left[1 + 1.5363 \times 10^{-3} \exp(-2.133 \times 10^{-4} H_a) \delta N_s \right]}{\sin(\theta_{nu}^{as} + 6.11 \times 10^{-3} \text{ rad})} \exp(-1.509 \times 10^{-4} H_a) \text{ m}, \quad (G.56)$$

for $H_a \geq 1,500\text{m}$, where

$$\delta N_s = 3.61 \times 10^{-3} H_a \cos \left[2\pi \left(\frac{d-152}{365} \right) \right] + \left\{ 0.1 \cos \left[2\pi \left(\frac{d-213}{365} \right) \right] - 0.8225 \right\} |L_a| \quad (G.57)$$

in the northern hemisphere and

$$\delta N_s = 3.61 \times 10^{-3} H_a \cos \left[2\pi \left(\frac{d-335}{365} \right) \right] + \left\{ 0.1 \cos \left[2\pi \left(\frac{d-30}{365} \right) \right] - 0.8225 \right\} |L_a| \quad (G.58)$$

in the southern hemisphere, where d is the day of year .

G.7.5 University of New Brunswick 3 Troposphere Delay Model

In the UNB3 troposphere delay model, the pressure, p , temperature, T , water vapor pressure, e , temperature lapse rate, β , and water vapor lapse rate, λ , are all predicted as a function of latitude and day of year, d , using [56, 57]

$$\begin{aligned} p &= p_0(L_a) + p_\sigma(L_a) \cos[2\pi(d - d_{\min})/365.25] \\ T &= T_0(L_a) + T_\sigma(L_a) \cos[2\pi(d - d_{\min})/365.25] \\ e &= e_0(L_a) + e_\sigma(L_a) \cos[2\pi(d - d_{\min})/365.25] , \\ \beta &= \beta_0(L_a) + \beta_\sigma(L_a) \cos[2\pi(d - d_{\min})/365.25] \\ \lambda &= \lambda_0(L_a) + \lambda_\sigma(L_a) \cos[2\pi(d - d_{\min})/365.25] \end{aligned} \quad (G.59)$$

where subscript 0 denotes the average value, subscript σ denotes the amplitude of the seasonal variation and d_{\min} is 28 in the northern hemisphere and 211 in the southern hemisphere. The UNB3 model provides values of each parameter at latitudes of $\pm 15^\circ$, 30° , 45° , 60° , and 75° . Tables G.2 and G.3 respectively list the average values and seasonal variation amplitudes of the meteorological parameters. Parameters at the required latitude are determined by interpolation using

$$\begin{aligned}
x(L_a) = & \begin{aligned} & x(15^\circ) & 180|L_a|/\pi \leq 15 \\ & (2 - 12|L_a|/\pi)x(15^\circ) + (12|L_a|/\pi - 1)x(30^\circ) & 15 \leq 180|L_a|/\pi \leq 30 \\ & (3 - 12|L_a|/\pi)x(30^\circ) + (12|L_a|/\pi - 2)x(45^\circ) & 30 \leq 180|L_a|/\pi \leq 45 \\ & (4 - 12|L_a|/\pi)x(45^\circ) + (12|L_a|/\pi - 3)x(60^\circ) & 45 \leq 180|L_a|/\pi \leq 60 \\ & (5 - 12|L_a|/\pi)x(60^\circ) + (12|L_a|/\pi - 4)x(75^\circ) & 60 \leq 180|L_a|/\pi \leq 75 \\ & x(75^\circ) & 75 \leq 180|L_a|/\pi \end{aligned} \\
& x \in p_0, T_0, e_0, \beta_0, \lambda_0, p_\sigma, T_\sigma, e_\sigma, \beta_\sigma, \lambda_\sigma
\end{aligned} \tag{G.60}$$

Table G.2 UNB3 Model Average Meteorological Parameters

| Latitude ($^\circ$) | p_0 (mbar) | T_0 (K) | e_0 (mbar) | β_0 (K/m) | λ_0 |
|-----------------------|--------------|-----------|--------------|-----------------------|-------------|
| 15 $^\circ$ | 1,013.25 | 299.65 | 26.31 | 6.30×10^{-3} | 2.77 |
| 30 $^\circ$ | 1,017.25 | 294.15 | 21.79 | 6.05×10^{-3} | 3.15 |
| 45 $^\circ$ | 1,015.75 | 283.15 | 11.66 | 5.58×10^{-3} | 2.57 |
| 60 $^\circ$ | 1,011.75 | 272.15 | 6.78 | 5.39×10^{-3} | 1.81 |
| 75 $^\circ$ | 1,013.00 | 263.65 | 4.11 | 4.53×10^{-3} | 1.55 |

Table G.3 UNB3 Model Seasonal Amplitudes of Meteorological Parameters

| Latitude ($^\circ$) | p_σ (mbar) | T_σ (K) | e_σ (mbar) | β_σ (K/m) | λ_σ |
|-----------------------|-------------------|----------------|-------------------|-----------------------|------------------|
| 15 $^\circ$ | 0.00 | 0.00 | 0.00 | 0.00×10^{-3} | 0.00 |
| 30 $^\circ$ | -3.75 | 7.00 | 8.85 | 0.25×10^{-3} | 0.33 |
| 45 $^\circ$ | -2.25 | 11.00 | 7.24 | 0.32×10^{-3} | 0.46 |
| 60 $^\circ$ | -1.75 | 15.00 | 5.36 | 0.81×10^{-3} | 0.74 |
| 75 $^\circ$ | -0.50 | 14.50 | 3.39 | 0.62×10^{-3} | 0.30 |

The dry and wet zenith delays are then calculated using

$$\delta\hat{\rho}_{TZd} = \left(1 - \frac{\beta H_a}{T}\right)^{\frac{g}{R_d \beta}} \left(\frac{k_1 R_d p}{g_m}\right), \tag{G.61}$$

$$\delta\hat{\rho}_{TZw} = \left(1 - \frac{\beta H_a}{T}\right)^{\frac{(\lambda+1)g}{R_d \beta}} \left(\frac{k_2 R_d p e}{[g_m(\lambda+1) - \beta R_d] T}\right), \tag{G.62}$$

where $g = 9.80665 \text{ m s}^{-2}$, $R_d = 287.054 \text{ J kg}^{-1} \text{ K}^{-1}$, $k_1 = 7.7604 \times 10^{-5} \text{ K mbar}^{-1}$, $g_m = 9.784 \text{ m s}^{-2}$, and $k_2 = 0.382 \text{ K}^2 \text{ mbar}^{-1}$.

Finally, the troposphere propagation delay for each individual signal is estimated using mapping functions, giving

$$\begin{aligned}
\delta\hat{\rho}_{T,a}^s = & \frac{\left[\sin^3 \theta_{nu}^{as} + (b_d + c_d) \sin \theta_{nu}^{as}\right] (1 + a_d + b_d + c_d + a_d c_d)}{\left[\sin^4 \theta_{nu}^{as} + (a_d + b_d + c_d) \sin^2 \theta_{nu}^{as} + a_d c_d\right] (1 + b_d + c_d)} \delta\hat{\rho}_{TZd} \\
& + \frac{\left[\sin^3 \theta_{nu}^{as} + (b_w + c_w) \sin \theta_{nu}^{as}\right] (1 + a_w + b_w + c_w + a_w c_w)}{\left[\sin^4 \theta_{nu}^{as} + (a_w + b_w + c_w) \sin^2 \theta_{nu}^{as} + a_w c_w\right] (1 + b_w + c_w)} \delta\hat{\rho}_{TZw}
\end{aligned} \tag{G.63}$$

where

$$\begin{aligned}
a_d &= 1.18972 \times 10^{-3} - 2.6855 \times 10^{-5} H_a + 1.0664 \times 10^{-4} \cos L_a \\
b_d &= 3.5716 \times 10^{-3} & c_d &= 8.2456 \times 10^{-2} \\
a_w &= 6.1120 \times 10^{-4} - 3.5348 \times 10^{-5} H_a + 1.526 \times 10^{-5} \cos L_a \\
b_w &= 1.8576 \times 10^{-3} & c_w &= 6.2741 \times 10^{-2}
\end{aligned} \tag{G.64}$$

G.8 Navigation Processor

This section describes alternative implementations of the position and signal geometry calculations, building on Section 9.4. Estimation of interconstellation timing biases is described first, followed by positioning using TDOA across satellites, use of delta-range measurements, and signal geometry with a chip-scale atomic clock.

G.8.1 Estimating Interconstellation Timing Biases

Where a multiconstellation GNSS position solution is required and up-to-date interconstellation timing biases have not been downloaded from the GNSS navigation data messages (or another source), it is necessary to estimate them as part of the navigation solution. These timing biases may be treated as constant in the short term, but are subject to possible step changes whenever there is an ephemeris update from one of the constellations. The single-epoch solution is described first, followed by the filtered solution and the dilution of precision calculation. A GPS/GLONASS solution is presented. However, the same principles apply for any combination of constellations.

If the receiver clock offset, $\delta\rho_c^a$, is estimated with respect to GPS time, the GLONASS–GPS time offset, $\delta\rho_c^{GL}$, must also be estimated. With an extra state, the minimum number of measurements required increases from 4 to 5. The linearized ECI-frame measurement model, (9.130), becomes

$$\begin{pmatrix} \tilde{\rho}_{a,C}^1 - \hat{\rho}_{a,C}^{1-} \\ \tilde{\rho}_{a,C}^2 - \hat{\rho}_{a,C}^{2-} \\ \vdots \\ \tilde{\rho}_{a,C}^m - \hat{\rho}_{a,C}^{m-} \end{pmatrix} = \mathbf{H}_G^i \begin{pmatrix} \hat{\mathbf{r}}_{ia}^{i+} - \hat{\mathbf{r}}_{ia}^{i-} \\ \hat{\mathbf{y}}_{ia}^{i+} - \hat{\mathbf{y}}_{ia}^{i-} \\ \hat{\mathbf{z}}_{ia}^{i+} - \hat{\mathbf{z}}_{ia}^{i-} \\ \delta\hat{\rho}_c^{a+} - \delta\hat{\rho}_c^{a-} \\ \delta\hat{\rho}_c^{GL+} - \delta\hat{\rho}_c^{GL-} \end{pmatrix} + \begin{pmatrix} \delta\rho_{a,\varepsilon}^{1+} \\ \delta\rho_{a,\varepsilon}^{2+} \\ \vdots \\ \delta\rho_{a,\varepsilon}^{m+} \end{pmatrix}. \quad (\text{G.65})$$

The predicted pseudo-range for the j^{th} measurement then becomes

$$\hat{\rho}_{a,C}^{j-} = \sqrt{[\hat{\mathbf{r}}_{ij}^i(\tilde{\mathbf{t}}_{st,a}^j) - \hat{\mathbf{r}}_{ia}^{i-}(\tilde{\mathbf{t}}_{sa,a}^j)]^T [\hat{\mathbf{r}}_{ij}^i(\tilde{\mathbf{t}}_{st,a}^j) - \hat{\mathbf{r}}_{ia}^{i-}(\tilde{\mathbf{t}}_{sa,a}^j)]} + \delta\hat{\rho}_c^{a-} - \delta_{j \in GL} \delta\hat{\rho}_c^{GL-} \quad (\text{G.66})$$

and the measurement matrix becomes

$$\mathbf{H}_G^i = \begin{pmatrix} -u_{a1,x}^i & -u_{a1,y}^i & -u_{a1,z}^i & 1 & -\delta_{1 \in GL} \\ -u_{a2,x}^i & -u_{a2,y}^i & -u_{a2,z}^i & 1 & -\delta_{2 \in GL} \\ \vdots & \vdots & \vdots & \vdots & \vdots \\ -u_{am,x}^i & -u_{am,y}^i & -u_{am,z}^i & 1 & -\delta_{m \in GL} \end{pmatrix}_{\mathbf{r}_{ia}^i - \hat{\mathbf{r}}_{ia}^{i-}}, \quad (\text{G.67})$$

where $\delta_{j \in GL}$ is 1 where j is a GLONASS signal and 0 otherwise. The negative sign convention matches that of the satellite clock offset from system time (Section 9.3.1).

The weighted least-squares position and time estimate is then

$$\begin{pmatrix} \hat{\mathbf{r}}_{ia}^{i+} \\ \delta\hat{\rho}_c^{a+} \\ \delta\hat{\rho}_c^{GL+} \end{pmatrix} = \begin{pmatrix} \hat{\mathbf{r}}_{ia}^{i-} \\ \delta\hat{\rho}_c^{a-} \\ \delta\hat{\rho}_c^{GL-} \end{pmatrix} + \left(\mathbf{H}_G^{i\ T} \mathbf{C}_\rho^{-1} \mathbf{H}_G^i \right)^{-1} \mathbf{H}_G^{i\ T} \mathbf{C}_\rho^{-1} \begin{pmatrix} \tilde{\rho}_{a,C}^1 - \hat{\rho}_{a,C}^{1-} \\ \tilde{\rho}_{a,C}^2 - \hat{\rho}_{a,C}^{2-} \\ \vdots \\ \tilde{\rho}_{a,C}^m - \hat{\rho}_{a,C}^{m-} \end{pmatrix}, \quad (\text{G.68})$$

The ECEF-frame equivalent is

$$\begin{pmatrix} \hat{\mathbf{r}}_{ea}^{e+} \\ \delta\hat{\rho}_c^{a+} \\ \delta\hat{\rho}_c^{GL+} \end{pmatrix} = \begin{pmatrix} \hat{\mathbf{r}}_{ea}^{e-} \\ \delta\hat{\rho}_c^{a-} \\ \delta\hat{\rho}_c^{GL-} \end{pmatrix} + \left(\mathbf{H}_G^e \mathbf{C}_\rho^{-1} \mathbf{H}_G^e \right)^{-1} \mathbf{H}_G^e \mathbf{C}_\rho^{-1} \begin{pmatrix} \tilde{\rho}_{a,C}^1 - \hat{\rho}_{a,C}^{1-} \\ \tilde{\rho}_{a,C}^2 - \hat{\rho}_{a,C}^{2-} \\ \vdots \\ \tilde{\rho}_{a,C}^m - \hat{\rho}_{a,C}^{m-} \end{pmatrix}, \quad (\text{G.69})$$

where

$$\hat{\rho}_{a,C}^{j-} = \sqrt{\left[\hat{\mathbf{r}}_{ej}^e(\tilde{t}_{st,a}^j) - \hat{\mathbf{r}}_{ea}^{e-}(\tilde{t}_{sa,a}^j) \right]^T \left[\hat{\mathbf{r}}_{ej}^e(\tilde{t}_{st,a}^j) - \hat{\mathbf{r}}_{ea}^{e-}(\tilde{t}_{sa,a}^j) \right]} + \delta\hat{\rho}_c^{a-} - \delta_{j \in GL} \delta\hat{\rho}_c^{GL-} \quad (\text{G.70})$$

or

$$\hat{\rho}_{a,C}^{j-} = \sqrt{\left[\mathbf{C}_e^I(\tilde{t}_{st,a}^j) \hat{\mathbf{r}}_{ej}^e(\tilde{t}_{st,a}^j) - \hat{\mathbf{r}}_{ea}^{e-}(\tilde{t}_{sa,a}^j) \right]^T \left[\mathbf{C}_e^I(\tilde{t}_{st,a}^j) \hat{\mathbf{r}}_{ej}^e(\tilde{t}_{st,a}^j) - \hat{\mathbf{r}}_{ea}^{e-}(\tilde{t}_{sa,a}^j) \right]} + \delta\hat{\rho}_c^{a-} - \delta_{j \in GL} \delta\hat{\rho}_c^{GL-} \quad (\text{G.71})$$

and

$$\mathbf{H}_G^e = \begin{pmatrix} -u_{a1,x}^e & -u_{a1,y}^e & -u_{a1,z}^e & 1 & -\delta_{1 \in GL} \\ -u_{a2,x}^e & -u_{a2,y}^e & -u_{a2,z}^e & 1 & -\delta_{2 \in GL} \\ \vdots & \vdots & \vdots & \vdots & \vdots \\ -u_{am,x}^e & -u_{am,y}^e & -u_{am,z}^e & 1 & -\delta_{m \in GL} \end{pmatrix}_{\mathbf{r}_{ia}^i = \hat{\mathbf{r}}_{ia}^{i-}}. \quad (\text{G.72})$$

The least-squares velocity and clock drift solution is unaffected by interconstellation timing biases.

For the filtered navigation solution, the GLONASS–GPS time offset, $\delta\rho_c^{GL}$, is added to the state vector, so (9.145) becomes

$$\mathbf{x}^i = \begin{pmatrix} \mathbf{r}_{ia}^i \\ \mathbf{v}_{ia}^i \\ \delta\rho_c^a \\ \delta\dot{\rho}_c^a \\ \delta\rho_c^{GL} \end{pmatrix}, \quad \mathbf{x}^e = \begin{pmatrix} \mathbf{r}_{ea}^e \\ \mathbf{v}_{ea}^e \\ \delta\rho_c^a \\ \delta\dot{\rho}_c^a \\ \delta\rho_c^{GL} \end{pmatrix}, \quad \mathbf{x}^n = \begin{pmatrix} L_a \\ \lambda_a \\ h_a \\ \mathbf{v}_{ea}^e \\ \delta\rho_c^a \\ \delta\dot{\rho}_c^a \\ \delta\rho_c^{GL} \end{pmatrix}. \quad (\text{G.73})$$

The time offset is assumed constant, so the state dynamics are

$$\mathbf{E}(\delta\dot{\rho}_c^{GL}) = 0, \quad (\text{G.74})$$

giving an overall system matrix of

$$\mathbf{F}^i = \mathbf{F}^e = \begin{pmatrix} \mathbf{0}_3 & \mathbf{I}_3 & \mathbf{0}_{3,1} & \mathbf{0}_{3,1} & \mathbf{0}_{3,1} \\ \mathbf{0}_3 & \mathbf{0}_3 & \mathbf{0}_{3,1} & \mathbf{0}_{3,1} & \mathbf{0}_{3,1} \\ \mathbf{0}_{1,3} & \mathbf{0}_{1,3} & 0 & 1 & 0 \\ \mathbf{0}_{1,3} & \mathbf{0}_{1,3} & 0 & 0 & 0 \\ \mathbf{0}_{1,3} & \mathbf{0}_{1,3} & 0 & 0 & 0 \end{pmatrix}, \quad \mathbf{F}^n = \begin{pmatrix} \mathbf{0}_3 & \mathbf{F}_{12}^n & \mathbf{0}_{3,1} & \mathbf{0}_{3,1} & \mathbf{0}_{3,1} \\ \mathbf{0}_3 & \mathbf{0}_3 & \mathbf{0}_{3,1} & \mathbf{0}_{3,1} & \mathbf{0}_{3,1} \\ \mathbf{0}_{1,3} & \mathbf{0}_{1,3} & 0 & 1 & 0 \\ \mathbf{0}_{1,3} & \mathbf{0}_{1,3} & 0 & 0 & 0 \\ \mathbf{0}_{1,3} & \mathbf{0}_{1,3} & 0 & 0 & 0 \end{pmatrix}. \quad (\text{G.75})$$

The system noise covariance for the GPS–GLONASS time-offset state should normally be set very small, sufficient to compensate for numerical rounding errors (see Section 3.3.3). However, a larger value, such as $(10\text{m})^2$, should be used whenever there is an ephemeris update.

In the EKF measurement model, the predicted pseudo-ranges become

$$\hat{\rho}_{a,C,k}^{j-} = \sqrt{\left[\hat{\mathbf{r}}_{ij}^i(\tilde{t}_{st,a,k}^j) - \hat{\mathbf{r}}_{ia,k}^{i-} \right]^T \left[\hat{\mathbf{r}}_{ij}^i(\tilde{t}_{st,a,k}^j) - \hat{\mathbf{r}}_{ia,k}^{i-} \right]} + \delta \hat{\rho}_{c,k}^{a-} - \delta_{j \in GL} \delta \hat{\rho}_{c,k}^{GL-}, \quad (\text{G.76})$$

$$\hat{\rho}_{a,C,k}^{j-} = \sqrt{\left[\hat{\mathbf{r}}_{ej}^e(\tilde{t}_{st,a,k}^j) - \hat{\mathbf{r}}_{ea,k}^{e-} \right]^T \left[\hat{\mathbf{r}}_{ej}^e(\tilde{t}_{st,a,k}^j) - \hat{\mathbf{r}}_{ea,k}^{e-} \right]} + \delta \hat{\rho}_{c,k}^{a-} - \delta_{j \in GL} \delta \hat{\rho}_{c,k}^{GL-} + \delta \rho_{ie}^j, \quad (\text{G.77})$$

or

$$\hat{\rho}_{a,C,k}^{j-} = \sqrt{\left[\mathbf{C}_e^T(\tilde{t}_{st,a,k}^j) \hat{\mathbf{r}}_{ej}^e(\tilde{t}_{st,a,k}^j) - \hat{\mathbf{r}}_{ea,k}^{e-} \right]^T \left[\mathbf{C}_e^T(\tilde{t}_{st,a,k}^j) \hat{\mathbf{r}}_{ej}^e(\tilde{t}_{st,a,k}^j) - \hat{\mathbf{r}}_{ea,k}^{e-} \right]} + \delta \hat{\rho}_{c,k}^{a-} - \delta_{j \in GL} \delta \hat{\rho}_{c,k}^{GL-}, \quad (\text{G.78})$$

noting that the predicted pseudo-range rates are unchanged from Section 9.4.2.3.

The measurement matrix for the ECI-frame implementation becomes

$$\mathbf{H}_{G,k}^i \approx \begin{pmatrix} -u_{a1,x}^i & -u_{a1,y}^i & -u_{a1,z}^i & 0 & 0 & 0 & 1 & 0 & -\delta_{1 \in GL} \\ -u_{a2,x}^i & -u_{a2,y}^i & -u_{a2,z}^i & 0 & 0 & 0 & 1 & 0 & -\delta_{2 \in GL} \\ \vdots & \vdots & \vdots & \vdots & \vdots & \vdots & \vdots & \vdots & \vdots \\ -u_{am,x}^i & -u_{am,y}^i & -u_{am,z}^i & 0 & 0 & 0 & 1 & 0 & -\delta_{m \in GL} \\ \hline 0 & 0 & 0 & -u_{a1,x}^i & -u_{a1,y}^i & -u_{a1,z}^i & 0 & 1 & 0 \\ 0 & 0 & 0 & -u_{a2,x}^i & -u_{a2,y}^i & -u_{a2,z}^i & 0 & 1 & 0 \\ \vdots & \vdots & \vdots & \vdots & \vdots & \vdots & \vdots & \vdots & \vdots \\ 0 & 0 & 0 & -u_{am,x}^i & -u_{am,y}^i & -u_{am,z}^i & 0 & 1 & 0 \end{pmatrix}_{\mathbf{x}=\hat{\mathbf{x}}_k^-}, \quad (\text{G.79})$$

while the ECEF-frame measurement matrix, $\mathbf{H}_{G,k}^e$, is as $\mathbf{H}_{G,k}^i$ with \mathbf{u}_{aj}^e substituted for \mathbf{u}_{aj}^i .

The local-navigation-frame measurement matrix becomes.

$$\mathbf{H}_{G,k}^n \approx \begin{pmatrix} h_L u_{a1,N}^n & h_\lambda u_{a1,E}^n & u_{a1,D}^n & 0 & 0 & 0 & 1 & 0 & -\delta_{1 \in GL} \\ h_L u_{a2,N}^n & h_\lambda u_{a2,E}^n & u_{a2,D}^n & 0 & 0 & 0 & 1 & 0 & -\delta_{2 \in GL} \\ \vdots & \vdots & \vdots & \vdots & \vdots & \vdots & \vdots & \vdots & \vdots \\ h_L u_{am,N}^n & h_\lambda u_{am,E}^n & u_{am,D}^n & 0 & 0 & 0 & 1 & 0 & -\delta_{m \in GL} \\ \hline 0 & 0 & 0 & -u_{a1,N}^n & -u_{a1,E}^n & -u_{a1,D}^n & 0 & 1 & 0 \\ 0 & 0 & 0 & -u_{a2,N}^n & -u_{a2,E}^n & -u_{a2,D}^n & 0 & 1 & 0 \\ \vdots & \vdots & \vdots & \vdots & \vdots & \vdots & \vdots & \vdots & \vdots \\ 0 & 0 & 0 & -u_{am,N}^n & -u_{am,E}^n & -u_{am,D}^n & 0 & 1 & 0 \end{pmatrix}_{\mathbf{x}=\hat{\mathbf{x}}_k^-}, \quad (\text{G.80})$$

where h_L and h_λ are given by (9.167). The measurement noise covariance (Section 9.4.2.4) is also unchanged.

The cofactor matrices with the interconstellation timing bias, used to determine the DOP, are

$$\mathbf{\Pi}^n = \begin{pmatrix} D_N^2 & \cdot & \cdot & \cdot & \cdot \\ \cdot & D_E^2 & \cdot & \cdot & \cdot \\ \cdot & \cdot & D_V^2 & \cdot & \cdot \\ \cdot & \cdot & \cdot & D_T^2 & \cdot \\ \cdot & \cdot & \cdot & \cdot & D_I^2 \end{pmatrix} = \left(\mathbf{H}_G^{nC^T} \mathbf{H}_G^{nC} \right)^{-1} \quad (\text{G.81})$$

where $\mathbf{H}_{G,k}^{nC}$, is as $\mathbf{H}_{G,k}^i$ with \mathbf{u}_{aj}^n substituted for \mathbf{u}_{aj}^i , and

$$\mathbf{\Pi}^\gamma = \begin{pmatrix} D_x^2 & \cdot & \cdot & \cdot & \cdot \\ \cdot & D_y^2 & \cdot & \cdot & \cdot \\ \cdot & \cdot & D_z^2 & \cdot & \cdot \\ \cdot & \cdot & \cdot & D_T^2 & \cdot \\ \cdot & \cdot & \cdot & \cdot & D_I^2 \end{pmatrix} = \left(\mathbf{H}_G^\gamma \mathbf{H}_G^\gamma \right)^{-1} \quad \gamma \in i, e, \quad (\text{G.82})$$

where D_I is the interconstellation timing bias DOP. Estimating the interconstellation timing bias increases the DOP of the position and receiver clock offset estimates. With signals from m satellites, there exists a combination of $m-1$ satellites that will give the same position and receiver clock offset DOPs when the interconstellation timing bias is not estimated. Furthermore, if only one of the satellites used is a GLONASS satellite (or only one is a GPS satellite), that satellite's signal will not contribute at all to a single-epoch position and receiver clock offset solution. Instead, the information from that pseudo-range measurement will be used for the estimation of the interconstellation timing bias alone.

Thus, where the interconstellation timing bias is unknown and must thus be estimated, signals from at least two satellites from that constellation must be used in order for them to make a useful contribution to the navigation solution.

An alternative formulation for the least-squares single-epoch solution and the DOP analysis may be found in [58].

G.8.2 Time Difference of Arrival across Satellites

A GNSS navigation solution may be determined using TDOA across satellites, also known as hyperbolic positioning (see Section 7.1.4.2). A weighted least-squares position solution may be determined from m pseudo-range measurements using

$$\hat{\mathbf{r}}_{\beta a}^{\beta+} = \hat{\mathbf{r}}_{\beta a}^{\beta-} + \left(\mathbf{H}_G^{\Delta\beta} \mathbf{C}_\rho^{\Delta-1} \mathbf{H}_G^{\Delta\beta} \right)^{-1} \mathbf{H}_G^{\Delta\beta} \mathbf{C}_\rho^{\Delta-1} (\Delta \tilde{\mathbf{p}}_{a,C} - \Delta \hat{\mathbf{p}}_{a,C}), \quad \beta \in i, e, \quad (\text{G.83})$$

where

$$\Delta \tilde{\mathbf{p}}_{a,C} = \mathbf{D}_G \begin{pmatrix} \tilde{\rho}_{a,C}^1 \\ \tilde{\rho}_{a,C}^2 \\ \vdots \\ \tilde{\rho}_{a,C}^m \end{pmatrix}, \quad \Delta \hat{\mathbf{p}}_{a,C} = \mathbf{D}_G \begin{pmatrix} \hat{\rho}_{a,C}^{1-} \\ \hat{\rho}_{a,C}^{2-} \\ \vdots \\ \hat{\rho}_{a,C}^{m-} \end{pmatrix} \quad (\text{G.84})$$

$$\mathbf{H}_G^{\Delta\beta} = \mathbf{D}_G \mathbf{H}_G^\beta, \quad \mathbf{C}_\rho^{\Delta+} = \mathbf{D}_G \mathbf{C}_\rho^\beta \mathbf{D}_G^T$$

and \mathbf{D}_G is the $(m-1) \times m$ differencing matrix, each row of which comprises one element of value 1 and one element of value -1 , with the remaining elements zero. Note that the measurement error covariance matrix, \mathbf{C}_ρ^Δ , is not diagonal. This will produce the same single-epoch position solution as the conventional least-squares solution described in Section 9.4.1, but without estimating the receiver clock offset. A similar approach may be used to determine the velocity from pseudo-range-rate measurements.

A filtered TDOA EKF navigation solution may be formulated using a differenced measurement innovation, measurement matrix, and measurement noise covariance matrix in a conventional EKF algorithm. The clock offset and drift are omitted from the state vector, system matrix, transition matrix, and system noise covariance matrix. The differenced vectors and matrices, denoted by the superscript Δ , are related to their undifferenced counterparts by

$$\begin{aligned} \delta \mathbf{z}_{G,k}^{\Delta-} &= \mathbf{D}_{G,k} \delta \mathbf{z}_{G,k}^- \\ \mathbf{H}_{G,k}^{\Delta\gamma} &= \mathbf{D}_{G,k} \mathbf{H}_{G,k}^\gamma \quad \gamma \in i, e, n, \\ \mathbf{R}_{G,k}^\Delta &= \mathbf{D}_{G,k} \mathbf{R}_{G,k} \mathbf{D}_{G,k}^T \end{aligned} \quad (\text{G.85})$$

where each column of the differencing matrix, $\mathbf{D}_{G,k}$, corresponds to an undifferenced measurement and each row to a differenced measurement. If m pseudo-range and m pseudo-range-rate measurements are differenced, $\mathbf{D}_{G,k}$ will be a $(2m - 1) \times 2m$ matrix. Note that the measurement noise covariance matrix, $\mathbf{R}_{G,k}^\Delta$, is not diagonal and the clock offset and drift columns of the measurement matrix, $\mathbf{H}_{G,k}^\gamma$, are omitted.

A TDOA EKF will not produce the same position and velocity estimates as its passive-ranging counterpart. For navigation applications, these will generally be slightly noisier because the smoothing effect resulting from the receiver clock being more predictable than the user dynamics is lost. Furthermore, there is no clock coasting when signals from fewer than four satellites are tracked. However, a TDOA implementation is more robust against receiver clock discontinuities.

G.8.3 Using Delta-Range Measurements

The pseudo-range-rate measurements in a filtered navigation solution maybe replaced by delta-range measurements. The delta ranges, defined by (9.73), are the changes in ADR. They are less noisy than the pseudo-range rates where the measurement-update interval is much longer than the carrier tracking-loop correlation time. This applies with a 1s update interval and carrier phase tracking. Conversely, carrier frequency tracking, which can only produce pseudo-range rates, not delta ranges, is more robust.

Using delta ranges, the measurement vector is

$$\mathbf{z}_G = \{\tilde{\rho}_{a,C}^1, \tilde{\rho}_{a,C}^2, \dots, \tilde{\rho}_{a,C}^m, \mid \Delta\tilde{\rho}_{a,C}^1, \Delta\tilde{\rho}_{a,C}^2, \dots, \Delta\tilde{\rho}_{a,C}^m\}, \quad (\text{G.86})$$

where the corrections applied to the raw delta ranges from (9.73) comprise the time-differenced satellite clock corrections. The predicted measurements, used to determine the measurement innovation using (9.159), are given by

$$\mathbf{h}_G(\hat{\mathbf{x}}_k^-, \hat{\mathbf{x}}_{k-1}^+) = \left(\hat{\rho}_{a,C,k}^{1-}, \hat{\rho}_{a,C,k}^{2-}, \dots, \hat{\rho}_{a,C,k}^{m-}, \mid \left[\hat{\rho}_{a,C,k}^{1-} - \hat{\rho}_{a,C,k-1}^{1+} \right], \left[\hat{\rho}_{a,C,k}^{2-} - \hat{\rho}_{a,C,k-1}^{2+} \right], \dots, \left[\hat{\rho}_{a,C,k}^{m-} - \hat{\rho}_{a,C,k-1}^{m+} \right] \right) \quad (\text{G.87})$$

where it is assumed that the time interval over which the ADRs are differenced to form the delta-range measurements is the same as the Kalman filter system propagation and measurement update intervals. The predicted pseudo-ranges are calculated as described in Section 9.4.2.3, noting that the values from the previous EKF iteration are calculated using the updated state vector estimate, $\hat{\mathbf{x}}_{k-1}^+$, not $\hat{\mathbf{x}}_{k-1}^-$.

Using the second method described in Section 3.3.4, the measurement matrix is

$$\mathbf{H}_{G,k}^\gamma = \begin{pmatrix} \mathbf{H}_{\rho,k}^\gamma \\ \mathbf{H}_{\rho,k}^\gamma [\mathbf{I} - \Phi_{k-1}^\gamma] \end{pmatrix}, \quad \gamma \in i, e, n \quad (\text{G.88})$$

where

$$\mathbf{H}_{\rho,k}^\gamma \approx \begin{pmatrix} -u_{a1,x}^\gamma & -u_{a1,y}^\gamma & -u_{a1,z}^\gamma & 0 & 0 & 0 & 1 & 0 \\ -u_{a2,x}^\gamma & -u_{a2,y}^\gamma & -u_{a2,z}^\gamma & 0 & 0 & 0 & 1 & 0 \\ \vdots & \vdots & \vdots & \vdots & \vdots & \vdots & \vdots & \vdots \\ -u_{am,x}^\gamma & -u_{am,y}^\gamma & -u_{am,z}^\gamma & 0 & 0 & 0 & 1 & 0 \end{pmatrix}_{\mathbf{x}=\hat{\mathbf{x}}_k^-} \quad \gamma \in i, e, \quad (\text{G.89})$$

$$\mathbf{H}_{\rho,k}^n \approx \begin{pmatrix} h_L u_{a1,N}^n & h_\lambda u_{a1,E}^n & u_{a1,D}^n & 0 & 0 & 0 & 1 & 0 \\ h_L u_{a2,N}^n & h_\lambda u_{a2,E}^n & u_{a2,D}^n & 0 & 0 & 0 & 1 & 0 \\ \vdots & \vdots & \vdots & \vdots & \vdots & \vdots & \vdots & \vdots \\ h_L u_{am,N}^n & h_\lambda u_{am,E}^n & u_{am,D}^n & 0 & 0 & 0 & 1 & 0 \end{pmatrix}_{\mathbf{x}=\hat{\mathbf{x}}_k^-}. \quad (\text{G.90})$$

G.8.4 Signal Geometry with a Chip-Scale Atomic Clock

Using a CSAC (or any other atomic frequency standard), the receiver clock offset is highly stable, as discussed in Section 9.1.2. Consequently, when the signal geometry is poor, a recent clock offset solution from when the geometry was better may be used to aid positioning. A position solution may even be obtained using signals from only three satellites. An EKF-based navigation filter will do this implicitly, while additional algorithms are required for a single-epoch solution.

Precise modeling of the effect of this on positioning accuracy is complex. However, an approximate DOP may be calculated by assuming that the clock offset is available as a pseudo-measurement of the same accuracy as the pseudo-range measurements and with independent errors. The cofactor matrix is then given by

$$\mathbf{\Pi}^n = \begin{pmatrix} D_N^2 & \cdot & \cdot & \cdot \\ \cdot & D_E^2 & \cdot & \cdot \\ \cdot & \cdot & D_V^2 & \cdot \\ \cdot & \cdot & \cdot & D_T^2 \end{pmatrix} \approx (\mathbf{H}_G'^{nC\text{T}} \mathbf{H}_G'^{nC})^{-1}, \quad (\text{G.91})$$

or

$$\mathbf{\Pi}^\gamma = \begin{pmatrix} D_x^2 & \cdot & \cdot & \cdot \\ \cdot & D_y^2 & \cdot & \cdot \\ \cdot & \cdot & D_z^2 & \cdot \\ \cdot & \cdot & \cdot & D_T^2 \end{pmatrix} \approx (\mathbf{H}_G'^{\gamma\text{T}} \mathbf{H}_G'^{\gamma})^{-1} \quad \gamma \in i, e, \quad (\text{G.92})$$

where

$$\mathbf{H}_G'^{\gamma} = \begin{pmatrix} \mathbf{H}_G^\gamma \\ 0 & 0 & 0 & 1 \end{pmatrix} \quad \gamma \in i, e, nC. \quad (\text{G.93})$$

Table G.4 DOPs with a CSAC and a Conventional Clock

| Example | Clock | NDOP | EDOP | VDOP | HDOP | PDOP |
|--|--------------|------|-------|------|-------|-------|
| 1: Optimal geometry | Conventional | 0.82 | 0.82 | 1.15 | 1.15 | 1.63 |
| | CSAC | 0.82 | 0.82 | 1.12 | 1.15 | 1.61 |
| 2: Lack of azimuth variation | Conventional | 1.63 | 10.56 | 8.90 | 10.68 | 13.91 |
| | CSAC | 1.63 | 1.81 | 2.04 | 2.44 | 3.18 |
| 3: High elevations | Conventional | 1.63 | 1.63 | 8.62 | 2.31 | 8.92 |
| | CSAC | 1.63 | 1.63 | 1.23 | 2.31 | 2.62 |
| 4: Reception only from opposing directions | Conventional | 1.45 | 8.21 | 2.15 | 8.34 | 8.61 |
| | CSAC | 1.45 | 8.21 | 1.24 | 8.34 | 8.43 |

For the geometry examples shown in Figures 9.32 to 9.35, Table G.4 compares the dilution of precision values obtained assuming a CSAC with those assuming a conventional clock. Table G.5 lists the satellite azimuth and elevation angles for these examples. A CSAC is thus predicted to bring significant accuracy improvements for cases such as Example 2 (Figure 9.33), where there is little variation in azimuth, and Example 3 (Figure 9.34), where the signals are all from high elevation satellites. However, in Example 1 (Figure 9.32), where the

geometry is optimal, and Example 4 (Figure 9.36), where signals are received from two opposing directions, the CSAC has little impact. In general, a CSAC is beneficial for geometries where it is difficult to separate one or more components of position from time.

Table G.5 Satellite Azimuth and Elevation Angles for Signal Geometry Examples

| Satellite | Example 1 | | Example 2 | | Example 3 | | Example 4 | |
|-----------|-----------|-----------|-----------|-----------|-----------|-----------|-----------|-----------|
| | Azimuth | Elevation | Azimuth | Elevation | Azimuth | Elevation | Azimuth | Elevation |
| 1 | 0° | 0° | 60° | 30° | 0° | 60° | 350° | 30° |
| 2 | 120° | 0° | 90° | 30° | 120° | 60° | 10° | 75° |
| 3 | 240° | 0° | 120° | 30° | 240° | 60° | 190° | 75° |
| 4 | 0° | 90° | 90° | 60° | 0° | 90° | 170° | 30° |

G.9 Integer Wavelength Ambiguity Resolution

This section provides additional information on integer wavelength ambiguity resolution, building on Section 10.2. The single-epoch and filtered geometry-based float solutions are described, followed by a discussion of the correlation properties of the resulting ambiguity estimates. This is followed by a simplified description of the LAMBDA integer ambiguity search method and a discussion on ambiguity validation. Finally, the properties of wide-lane ADR measurements are described.

G.9.1 Single-Epoch Float Solution

The single-epoch float solution is a position solution and set of double-differenced wavelength ambiguities jointly estimated from a single set of double-differenced pseudo-range and ADR measurements using weighted least-squares estimation. The wavelength ambiguities are assumed to be continuous rather than integers (or half integers). The pseudo-range or ADR measurements may be from a single epoch or averaged over a short interval to reduce noise. The averaging interval must be short enough for the line-of-sight vectors to be assumed constant, otherwise a more sophisticated float solution algorithm must be used. The pseudo-range measurements should not be smoothed using the ADR, so these are assumed to be independent from each other. It is also assumed here that the user and reference antennas are sufficiently close for the line of sight vectors to the two antennas to be considered parallel.

Assuming an ECEF reference frame and resolving axes, the state vector is defined as

$$\mathbf{x}^e = \begin{pmatrix} \mathbf{x}_G^e \\ \mathbf{x}_N \end{pmatrix} \quad \mathbf{x}_G^e = \mathbf{r}_{ra}^e \quad \mathbf{x}_N = \begin{pmatrix} \nabla \Delta N_{ra}^{t1,l} \\ \nabla \Delta N_{ra}^{t2,l} \\ \vdots \\ \nabla \Delta N_{ra}^{tm,l} \end{pmatrix}, \quad (\text{G.94})$$

where \mathbf{r}_{ra}^e is the relative position of the user antenna with respect to the reference antenna and \mathbf{x}_N is the vector of m wavelength ambiguities, noting that t is the reference satellite.

Assuming that the double-differenced pseudo-range measurements, ADR measurements, and ambiguity states are all listed in the same order, the weighted-least-squares solution is

$$\hat{\mathbf{x}}^+ = \hat{\mathbf{x}}^- + \left(\mathbf{H}_F^e \mathbf{C}_F^{\nabla \Delta -1} \mathbf{H}_F^e \right)^{-1} \mathbf{H}_F^e \mathbf{C}_F^{\nabla \Delta -1} \begin{pmatrix} \nabla \Delta \tilde{\rho}_{ra,R}^{t1,l} - \nabla \Delta \hat{r}_{ra}^{t1-} \\ \nabla \Delta \tilde{\rho}_{ra,R}^{t2,l} - \nabla \Delta \hat{r}_{ra}^{t2-} \\ \vdots \\ \nabla \Delta \tilde{\rho}_{ra,R}^{tm,l} - \nabla \Delta \hat{r}_{ra}^{tm-} \\ \hline \nabla \Delta \tilde{\Phi}_{ra,R}^{t1,l} - \nabla \Delta \hat{N}_{ra}^{t1,l} - \lambda_{ca}^l - \nabla \Delta \hat{r}_{ra}^{t1-} \\ \nabla \Delta \tilde{\Phi}_{ra,R}^{t2,l} - \nabla \Delta \hat{N}_{ra}^{t2,l} - \lambda_{ca}^l - \nabla \Delta \hat{r}_{ra}^{t2-} \\ \vdots \\ \nabla \Delta \tilde{\Phi}_{ra,R}^{tm,l} - \nabla \Delta \hat{N}_{ra}^{tm,l} - \lambda_{ca}^l - \nabla \Delta \hat{r}_{ra}^{tm-} \end{pmatrix}, \quad (\text{G.95})$$

where $\nabla\Delta\hat{r}_{ra}^{ts-}$ is the predicted double-differenced range, given by (10.16), $\nabla\Delta\tilde{\rho}_{ra,R}^{ts,l}$ and $\nabla\Delta\tilde{\phi}_{ra,R}^{ts,l}$ are, respectively, the double-differenced pseudo-range and ADR measurements; the measurement matrix, \mathbf{H}_F^e , is given by

$$\mathbf{H}_F^e = \begin{pmatrix} \mathbf{D}_G \mathbf{H}_{rG}^e & \mathbf{0} \\ \mathbf{D}_G \mathbf{H}_{rG}^e & \mathbf{I}_m \end{pmatrix}, \quad (\text{G.96})$$

where \mathbf{H}_{rG}^e and \mathbf{D}_G , are given by (10.18); and $\mathbf{C}_F^{\nabla\Delta}$ is the double-differenced error covariance matrix, given by

$$\mathbf{C}_F^{\nabla\Delta} = \begin{pmatrix} \mathbf{D}_G \mathbf{C}_\rho^\nabla \mathbf{D}_G^T & \mathbf{0} \\ \mathbf{0} & \mathbf{D}_G \mathbf{C}_\phi^\nabla \mathbf{D}_G^T \end{pmatrix}, \quad (\text{G.97})$$

where \mathbf{C}_ρ^∇ is the measurement error covariance matrix for the pseudo-range measurements and \mathbf{C}_ϕ^∇ is the measurement error covariance matrix for the ADR measurements, both differenced across receivers. The predicted values of the ambiguity states may be set to zero as they have a linear relationship with the measurements.

G.9.2 Filtered Float Solution

An EKF-based float filter estimates the relative position and velocity, together with the double-differenced wavelength ambiguities from a series of double-differenced pseudo-range and ADR measurements. The wavelength ambiguities are assumed to be continuous rather than integers (or half integers). Each set of pseudo-range or ADR measurements must be from a single epoch and the pseudo-range measurements should not be smoothed using the ADR. It is also assumed here that the user and reference antennas are sufficiently close for the line of sight vectors to the two antennas to be considered parallel. All notation is as defined as in Section G.9.1, except where stated otherwise. The EKF is described in Chapter 3.

Assuming an ECEF reference frame and resolving axes, the state vector is defined as

$$\mathbf{x}^e = \begin{pmatrix} \mathbf{x}_G^e \\ \mathbf{x}_N^e \end{pmatrix} \quad \mathbf{x}_G^e = \begin{pmatrix} \mathbf{r}_{ra}^e \\ \mathbf{v}_{ra}^e \end{pmatrix} \quad \mathbf{x}_N = \begin{pmatrix} \nabla\Delta N_{ra}^{t1,l} \\ \nabla\Delta N_{ra}^{t2,l} \\ \vdots \\ \nabla\Delta N_{ra}^{tm,l} \end{pmatrix}, \quad (\text{G.98})$$

where \mathbf{v}_{ra}^e is the relative position of the user antenna with respect to the reference antenna.

The transition matrix (see Section 9.4.2.2) is

$$\Phi_{k-1}^e = \begin{pmatrix} \Phi_G^e & \mathbf{0} \\ \mathbf{0} & \mathbf{I}_m \end{pmatrix} \quad \Phi_G^e = \begin{pmatrix} \mathbf{I}_3 & \mathbf{I}_3 \tau_s \\ \mathbf{0} & \mathbf{I}_3 \end{pmatrix}, \quad (\text{G.99})$$

where τ_s is the state propagation interval. The system noise covariance matrix is

$$\mathbf{Q}_{k-1}^e = \begin{pmatrix} \mathbf{Q}_{G,k-1}^e & \mathbf{0} \\ \mathbf{0} & Q_N \mathbf{I}_m \end{pmatrix}, \quad (\text{G.100})$$

where $\mathbf{Q}_{G,k-1}^e$ comprises the first six row and columns of (9.152) or (9.154). The wavelength ambiguities are assumed to be constant so, in theory, $Q_N = 0$. In practice, Q_N should be set to a very small value to compensate for the effect of numerical rounding errors (see Section 3.3.3).

The measurement innovations comprise the differences between the measured and predicted double-differenced pseudo-ranges and ADRs. Thus,

$$\delta \mathbf{z}_{F,k}^- = \begin{pmatrix} \nabla \Delta \tilde{\rho}_{ra,R}^{t1,l} - \nabla \Delta \hat{r}_{ra}^{t1-} \\ \nabla \Delta \tilde{\rho}_{ra,R}^{t2,l} - \nabla \Delta \hat{r}_{ra}^{t2-} \\ \vdots \\ \nabla \Delta \tilde{\rho}_{ra,R}^{tm,l} - \nabla \Delta \hat{r}_{ra}^{tm-} \\ \nabla \Delta \tilde{\Phi}_{ra,R}^{t1,l} - \nabla \Delta \hat{N}_{ra}^{t1,l-} \lambda_{ca}^l - \nabla \Delta \hat{r}_{ra}^{t1-} \\ \nabla \Delta \tilde{\Phi}_{ra,R}^{t2,l} - \nabla \Delta \hat{N}_{ra}^{t2,l-} \lambda_{ca}^l - \nabla \Delta \hat{r}_{ra}^{t2-} \\ \vdots \\ \nabla \Delta \tilde{\Phi}_{ra,R}^{tm,l} - \nabla \Delta \hat{N}_{ra}^{tm,l-} \lambda_{ca}^l - \nabla \Delta \hat{r}_{ra}^{tm-} \end{pmatrix}_k, \quad (\text{G.101})$$

where the predicted double-differenced range is given by

$$\nabla \Delta \hat{r}_{ra,k}^{ts-} = \left| \hat{\mathbf{r}}_{es}^e(\tilde{\mathbf{t}}_{st,a}^{s,l}) - \mathbf{r}_{er}^e - \hat{\mathbf{r}}_{ra,k}^{e-} \right| - \left| \hat{\mathbf{r}}_{et}^e(\tilde{\mathbf{t}}_{st,a}^{t,l}) - \mathbf{r}_{er}^e - \hat{\mathbf{r}}_{ra,k}^{e-} \right| - \left| \hat{\mathbf{r}}_{es}^e(\tilde{\mathbf{t}}_{st,r}^{s,l}) - \mathbf{r}_{er}^e \right| + \left| \hat{\mathbf{r}}_{et}^e(\tilde{\mathbf{t}}_{st,r}^{t,l}) - \mathbf{r}_{er}^e \right|, \quad (\text{G.102})$$

for differential positioning where the reference station position is known and constant, and

$$\nabla \Delta \hat{r}_{ra,k}^{ts-} = \left| \hat{\mathbf{r}}_{es}^e(\tilde{\mathbf{t}}_{st,a}^{s,l}) - \hat{\mathbf{r}}_{ea,k}^{e+} \right| - \left| \hat{\mathbf{r}}_{et}^e(\tilde{\mathbf{t}}_{st,a}^{t,l}) - \hat{\mathbf{r}}_{ea,k}^{e+} \right| - \left| \hat{\mathbf{r}}_{es}^e(\tilde{\mathbf{t}}_{st,r}^{s,l}) - \hat{\mathbf{r}}_{ea,k}^{e+} + \hat{\mathbf{r}}_{ra,k}^{e-} \right| + \left| \hat{\mathbf{r}}_{et}^e(\tilde{\mathbf{t}}_{st,r}^{t,l}) - \hat{\mathbf{r}}_{ea,k}^{e+} + \hat{\mathbf{r}}_{ra,k}^{e-} \right|, \quad (\text{G.103})$$

for relative positioning where the reference station position is unknown and $\hat{\mathbf{r}}_{ea,k}^{e+}$ is the stand-alone user position, obtained as described in Section 9.4.2.

The measurement matrix is

$$\mathbf{H}_F^e = \begin{pmatrix} \mathbf{D}_G \mathbf{H}_{rG}^e & \mathbf{0} & \mathbf{0} \\ \mathbf{D}_G \mathbf{H}_{rG}^e & \mathbf{0} & \mathbf{I}_m \end{pmatrix}, \quad (\text{G.104})$$

where \mathbf{H}_{rG}^e and \mathbf{D}_G are given by (10.18) and the sub-matrix columns correspond to the relative position, relative velocity, and double-differenced ambiguity states.

Finally, the measurement noise covariance matrix is

$$\mathbf{R}_F = \begin{pmatrix} \mathbf{D}_G \mathbf{R}_\rho^\nabla \mathbf{D}_G^\text{T} & \mathbf{0} \\ \mathbf{0} & \mathbf{D}_G \mathbf{R}_\Phi^\nabla \mathbf{D}_G^\text{T} \end{pmatrix}, \quad (\text{G.105})$$

where \mathbf{R}_ρ^∇ is the measurement noise covariance matrix for the pseudo-range measurements and \mathbf{R}_Φ^∇ is the measurement noise covariance matrix for the ADR measurements, both differenced across receivers.

After the ambiguities have been fixed, the float filter should continue to operate in order to maintain the relative position and velocity solutions. The ambiguity-fixed position and velocity are determined from their float counterparts using (10.21).

The float filter may also be augmented with states for the difference in each ionosphere propagation delay experienced at the user and reference receivers and the variation in troposphere refractivity [59].

G.9.3 Correlation Properties of the Geometry-Based Float Ambiguity Estimates

Consider the grossly simplified case of one-dimensional positioning using two double-differenced pseudo-ranges and the corresponding double-differenced ADRs (all lines of sight are parallel in the 1D case). The float solution comprises one position state and two wavelength ambiguity states. As there are four measurements but only three states, the errors in the state estimates are highly correlated. Furthermore as two of the measurements are precise, but the other two are not, two relationships between the states can be determined to high precision, but the absolute values cannot.

Figure G.5 shows the float solution and uncertainty bounds for the two ambiguity states. The confidence intervals for the individual ambiguity states each span several candidate integer-fixed solutions. Simply multiplying them together gives 20 candidate ambiguities for which a test statistic (given by (10.20)) must be evaluated. However, the combined confidence region, accounting for the correlation between the float ambiguity estimates, is much smaller. This is enclosed by the error ellipse in Figure G.5 and contains only three candidate ambiguities. This clearly shows the benefit of the geometry-based approach. Thus, if it can be determined which candidate ambiguities lie within this combined confidence region, the number of test statistics that must be computed is significantly reduced. Note that, in the example shown in the figure, the nearest candidate ambiguity pair to the float solution does not lie within the confidence region. Thus, simply fixing to the set of ambiguities nearest to the float solution often gives the wrong answer.

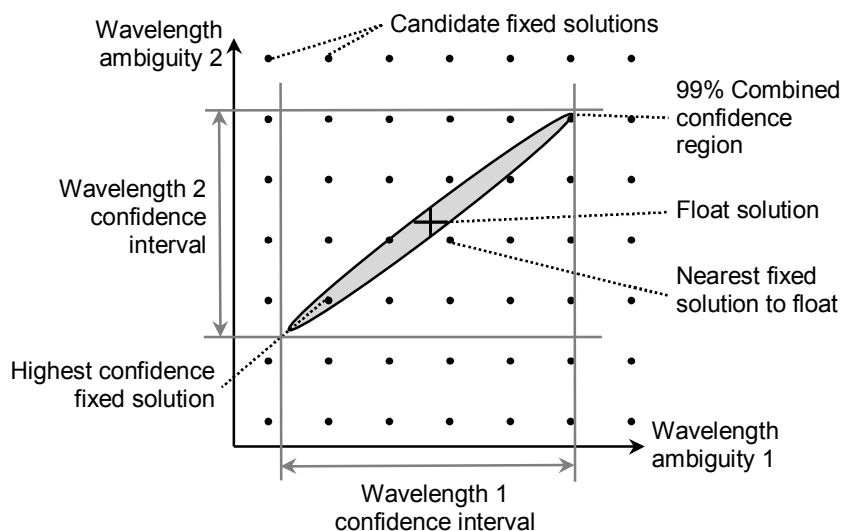


Figure G.5 Float solution and uncertainty bounds for two wavelength ambiguities.

Moving to the general case, for a single-epoch GNSS float solution with m ambiguities, there are m high-precision double-differenced ADR measurements, m low-precision double-differenced pseudo-range measurements and $m+3$ relative position and ambiguity states to estimate. Consequently, the error covariance matrix of the state estimates will have m small eigenvalues, reflecting the precision of the ADR measurements and 3 larger eigenvalues, reflecting the pseudo-range precision. The confidence region may be thought of as a $m+3$ -dimensional hyperellipsoid, which is large in 3 directions and small in the remaining m directions. However, the eigenvectors of the error covariance matrix or directions of the hyperellipsoid axes will not generally be aligned with the states. The same applies for a filtered navigation solution as the additional velocity states are the time derivatives of the position states, so are not independent. The challenge in fixing the ambiguities lies in determining which candidate sets lie within (or close to) the confidence region and which do not so that the number of test statistics that must be evaluated may be minimized.

G.9.4 The LAMBDA Method

The least-squares ambiguity decorrelation adjustment method works by aligning the axes of the ambiguity search space more closely with those of the confidence region obtained from the float solution [60, 61]. This is done by fixing linear combinations of the original set of ambiguities and then inferring the original ambiguities from the combinations. Figure G.6 shows how this may be used to reduce the search space in the two-ambiguity case. Here, a simplified description of the LAMBDA method is presented; a full description may be found in [62].

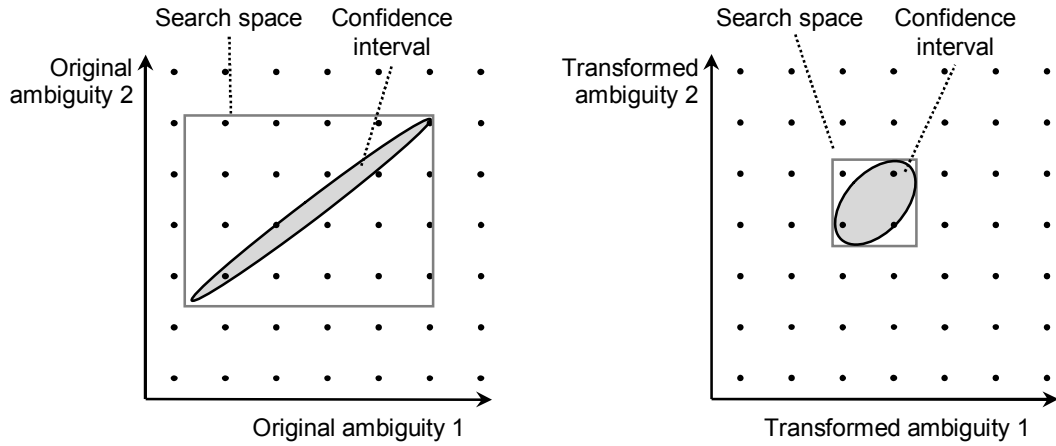


Figure G.6 Search space for two original and transformed ambiguities.

The float ambiguities and their covariance are transformed using

$$\hat{\mathbf{x}}_Z = \mathbf{Z}\hat{\mathbf{x}}_N \quad \mathbf{P}_Z = \mathbf{Z}\mathbf{P}_N\mathbf{Z}^T, \quad (\text{G.106})$$

where \mathbf{Z} is known as the decorrelation matrix. The reverse transformation, applied to the fixed ambiguities, is

$$\tilde{\mathbf{x}}_N = \mathbf{Z}^{-1}\tilde{\mathbf{x}}_Z \quad \mathbf{P}_N = \mathbf{Z}^{-1}\mathbf{P}_Z(\mathbf{Z}^{-1})^T. \quad (\text{G.107})$$

The decorrelation matrix is selected to meet the following conditions:

1. In the forward transformation, where the components of \mathbf{x}_N are all integers, the components of \mathbf{x}_Z must also be integers;
2. In the reverse transformation, where the components of \mathbf{x}_Z are all integers, the components of \mathbf{x}_N must also be integers;
3. The transformed float solution ambiguity error covariance, \mathbf{P}_Z , must be as close to diagonal as possible (without violating the other conditions). This minimizes the size of the search area.

The first condition is met by setting all components of \mathbf{Z} to integers, while the second condition is met by setting all components of \mathbf{Z}^{-1} to integers. From (A.35), applying the condition $|\mathbf{Z}| = \pm 1$ ensures that \mathbf{Z}^{-1} comprises integers whenever \mathbf{Z} comprises integers. Any triangular matrix with unit diagonal elements also has a unit determinant. To meet both this condition and the third, Cholesky factorization may be applied to the input error covariance matrix as described in Section A.6 of Appendix A, also on CD. Thus,

$$\mathbf{P}_N = \mathbf{L}\mathbf{D}_L\mathbf{L}^T, \quad (\text{G.108})$$

where \mathbf{L} is a lower triangular matrix with unit diagonal elements and \mathbf{D}_L is a diagonal matrix. From (G.107), to meet the third condition above the inverse of the decorrelation matrix, \mathbf{Z}^{-1} , should be set equal to \mathbf{L} and then its elements each rounded to the nearest integer to meet the first two conditions. Thus,

$$\mathbf{Z} = [\text{round}(\mathbf{L})]^{-1}. \quad (\text{G.109})$$

Once the decorrelation matrix has been determined and the ambiguities and their covariance transformed using (G.106), the search space for the transformed ambiguities, \mathbf{x}_Z , must be determined. A hyper-rectangular search space is defined. This is centered at the float solution and bounded by the standard deviations of the individual transformed ambiguities (given by the root diagonal elements of \mathbf{P}_Z) each multiplied by the confidence limit. The confidence limit is that of the chi-square distribution with the number of degrees of freedom

equal to the number of ambiguities to be determined. Some examples are given in Table B.3 of Appendix B, also on CD.

For each candidate ambiguity set within the search space, $\mathbf{x}_{Z,i}$, the test statistic

$$s_{Z,i}^2 = (\mathbf{x}_{Z,i} - \hat{\mathbf{x}}_Z)^T (\mathbf{P}_Z)^{-1} (\mathbf{x}_{Z,i} - \hat{\mathbf{x}}_Z) \quad (\text{G.110})$$

is computed. This has the same value as the test statistic for the corresponding original ambiguity set, $\mathbf{x}_{N,i}$, computed using (10.20). Whichever candidate set produces the smallest value of $s_{Z,i}^2$ is deemed the likeliest solution and transformed back to the original ambiguity space using (G.107).

G.9.5 Ambiguity Validation

As the float navigation and ambiguity solution is always contaminated by noise and other error sources, the set of ambiguities that is most consistent with the float solution will not always be the correct one. Therefore, validation should be performed to ensure that the ambiguity-fixed solution is sufficiently self-consistent and that there is no competing set of ambiguities that gives a similarly self-consistent solution.

The ambiguity set may be validated by computing navigation solutions from the ambiguity-fixed double-differenced ADR measurements using the likeliest and second likeliest set of ambiguities and determining the chi-square test statistic (see Section 17.4.1) from the measurement residuals of each solution using.

$$s_{\hat{\mathbf{z}}}^2 = \delta \mathbf{z}_k^{+T} \mathbf{C}_{\hat{\mathbf{z}},k}^{+ -1} \delta \mathbf{z}_k^{+}. \quad (\text{G.111})$$

The smaller this test statistic is, the more consistent the set of ambiguity-fixed measurements are and, thus, the more likely it is that the ambiguity fix is correct. The corresponding test statistics for other candidate ambiguities should be significantly larger. The ambiguity fix may be considered validated if the following conditions are met:

1. The chi-square test statistic for the likeliest ambiguity set is within a certain threshold;
2. The test statistic for the second likeliest ambiguity set exceeds a certain threshold;
3. The test statistic for the likeliest ambiguity divided by that for the second likeliest ambiguity is within a certain threshold.

Validation can also be performed in ambiguity space by comparing values of the ambiguity test statistic, $s_{Z,i}^2$, computed from different ambiguity sets.

G.9.6 Properties of Wide-lane Measurements

Wide-lane ADR measurements may be formed from measurements on two frequencies in order to make ambiguity resolution easier. The double-differenced wide-lane ADR, expressed as a range, is given by

$$\nabla \Delta \tilde{\Phi}_{ra,R}^{ts,wl} = \frac{f_{ca}^{\alpha} \nabla \Delta \tilde{\Phi}_{ra,R}^{ts,\alpha} - f_{ca}^{\beta} \nabla \Delta \tilde{\Phi}_{ra,R}^{ts,\beta}}{f_{ca}^{\alpha} - f_{ca}^{\beta}}, \quad (\text{G.112})$$

where $\nabla \Delta \tilde{\Phi}_{ra,R}^{ts,\alpha}$ and $\nabla \Delta \tilde{\Phi}_{ra,R}^{ts,\beta}$ are the corresponding single-frequency ADR measurements.

The wavelength ambiguities are related by

$$\nabla \Delta N_{ra}^{ts,wl} = \nabla \Delta N_{ra}^{ts,\alpha} - \nabla \Delta N_{ra}^{ts,\beta}, \quad (\text{G.113})$$

so if the ambiguities of the original measurements are integers, so is the ambiguity of the wide-lane measurement. Wide-lane measurements have a much larger wavelength of $c/(f_{ca}^{\alpha} - f_{ca}^{\beta})$, where f_{ca}^{α} and f_{ca}^{β} are the two carrier frequencies. This reduces the number of candidate values of the integer ambiguity. However, the measurement error standard deviation is increased to

$$\sigma_{\nabla\Delta\Phi}^{wl} = \frac{\sqrt{(f_{ca}^{\alpha}\sigma_{\nabla\Delta\Phi}^{\alpha})^2 + (f_{ca}^{\beta}\sigma_{\nabla\Delta\Phi}^{\beta})^2}}{f_{ca}^{\alpha} - f_{ca}^{\beta}} \quad (G.114)$$

where $\sigma_{\nabla\Delta\Phi}^{\alpha}$ and $\sigma_{\nabla\Delta\Phi}^{\beta}$ are the measurement error standard deviations of the original double-differenced ADR measurements. Table G.6 shows some examples, noting that GNSS wavelengths range between 0.19m for L1 and 0.26m for L5.

Table G.6 Wide-lane wavelengths and error standard deviations for selected frequency combinations

| <i>Frequency 1</i> | <i>Frequency 2</i> | <i>Wide-lane wavelength</i> | <i>Wide-lane to single-frequency noise ratio</i> |
|---------------------|----------------------|-----------------------------|--|
| 1575.42 MHz (L1/E1) | 1227.60 MHz (L2) | 0.86m | 5.74 |
| 1575.42 MHz (L1/E1) | 1176.45 MHz (L5/E5a) | 0.75m | 4.93 |
| 1227.60 MHz (L2) | 1176.45 MHz (L5/E5a) | 5.87m | 33.2 |
| 1207.14 MHz (E5b) | 1176.45 MHz (L5/E5a) | 9.78m | 54.9 |

G.10 Vector Tracking and Acquisition

This section discusses the vector phase lock loop (VPLL) and collective detection, a vectorized acquisition process.

G.10.1 Vector Phase Lock Loop

To implement carrier phase tracking with a combined navigation and tracking algorithm, in other words, a vector PLL, the pseudo-range rate measurement inputs to the VDFLL Kalman filter described in Section 10.3.7 are replaced by carrier phase measurements. The iteration rate must also be increased to accommodate the carrier-phase-tracking bandwidth, which is typically higher than the code tracking or carrier-frequency-tracking bandwidth.

Instead of separate code and carrier phase measurements, the Kalman filter may input the Is and Qs as its measurements directly [63]. The measurement matrix, \mathbf{H}_G , is obtained by differentiating (9.10). This is a form of coherent tracking, as the carrier phase must be known in order to track the code. Coherent tracking is less noisy and, in vector form, avoids discriminator nonlinearities. However, when there is insufficient signal to noise to track carrier phase, the code cannot be tracked either.

If the carrier phase error of each signal tracked is estimated as a Kalman filter state, carrier phase can be tracked without keeping the reference carrier phase within the receiver synchronized with that of the signal because the phase difference is then known. A measurement innovation may be formed from the difference between the carrier phase discriminator output and the value predicted from the Kalman filter estimates, noting that in conventional tracking, the predicted discriminator output is always zero.

However, the receiver's reference carrier frequency and code do need to be kept synchronized with the signal, otherwise the two do not correlate and the signal is absent from the I and Q measurements. Thus, the NCO command update rate and control lag must be designed to accommodate the code-tracking and carrier-frequency-tracking bandwidths necessary to respond to the user dynamics and the noise on the receiver's reference oscillator.

Adding carrier-phase states to the Kalman filter and iterating it at a higher rate significantly increases the processor load. A common solution is to use a bank of prefilters to track the carrier phase at a higher rate than the main navigation and tracking algorithm [64].

G.10.2 Collective Detection

Collective detection is an acquisition technique that operates on the same principle as vector tracking [65]. Signals are correlated individually at different code phases and Doppler shifts as for conventional acquisition (Section 9.2.1). FFT techniques may be used. However, the test statistics for signal detection are summed across all satellites to improve the signal to noise level. Only combinations that produce a consistent position, velocity, and receiver clock solution are considered. Thus, eight dimensions are searched.

A cold-start acquisition using this technique is not feasible. For GPS C/A code, there would be 2046 bins for the clock offset and each component of position, while with a 1ms coherent integration interval there would be 50 bins for the clock drift and each component of velocity. Thus, 10^{20} test statistics would need to be computed. By contrast, conventional acquisition of ten signals requires 10^6 test statistics to be computed. Furthermore, satellite ephemeris (or almanac) data and an approximate user position are required to determine the satellite velocities and lines of sight to enable position and velocity domain test statistics to be computed.

Collective detection is thus only applicable to warm-start acquisitions, including cases where assistance and aiding is available (see Section 10.5). Where the receiver clock drift has been calibrated and the user velocity is approximately known, the search may be limited to the position and clock offset domain only. For ± 10 km north and east search regions, a ± 200 m vertical search region and a ± 150 km (one C/A-code-length) clock offset search region, there are 6×10^8 test statistics to calculate. Performing an initial coarse search with neighboring code-phase bins averaged together reduces the number of test statistics at the expense of a reduction in sensitivity. Conversely, increasing the coherent integration interval to improve sensitivity reduces the Doppler bin spacing, so may require a search in the velocity and clock drift domain. Collective detection is thus best suited to scenarios where accurate aiding is available from other navigation sensors in order to limit the size of the search space.

G.11 Multipath and NLOS Mitigation

Multipath and NLOS reception mitigation techniques are reviewed in Section 10.4. This section summarizes some additional techniques, covering multipath mapping and techniques for reference stations.

G.11.1 Multipath Mapping

Where multipath errors are caused by reflections off the host-vehicle body, a given line-of-sight vector, resolved about the body frame, will always lead to the same multipath error. Therefore, by measuring the multipath error as a function of the line of sight, a map can be created which may then be used to calibrate out the multipath errors. This method has been successfully applied to carrier-phase multipath on a small spacecraft [66, 67]. Larger vehicles require higher-resolution maps for multipath calibration, while flexure of the host-vehicle body can render a map ineffective. An alternative approach is to map which lines of sight are susceptible to multipath and down-weight these measurements in the navigation solution.

G.11.2 Techniques for Reference Stations

Reference stations for differential positioning are normally static and there is typically more space available than on a vehicle or pedestrian. Consequently, additional multipath and NLOS reception mitigation techniques can be deployed.

Careful siting of the antenna is used to avoid reflections off nearby objects, so reflected signals tend to be of low or negative elevation. As a minimum, a choke ring antenna is used to attenuate these signals. However, an integrated multipath-limiting antenna (MLA) can be used to attenuate low-elevation-angle signals further by combining a high-zenith antenna (HZA) with a 14-element vertical antenna array [68]. The system is about 3m tall.

A further technique suitable for permanent fixed installations is sidereal filtering. This exploits the repetition of the lines of sight every ground-track repeat period (See Table 8.14), which is 1 sidereal day for GPS. Multipath interference and any NLOS signal reception will also repeat with the same period. Consequently, measurements of previous multipath-induced errors can be used to predict the current errors and thus correct the measurements made by the reference station [69].

G.12 Positioning using Ambiguous Pseudo-ranges

Where there is insufficient C/N_0 to decode the navigation data message, it cannot be used to resolve the ambiguity in the pseudo-range measurements due to the code repetition period (see Section 9.2.7). This is 300 km for GPS and GLONASS C/A code. If the navigation data message bit edges are detectable but the message cannot be decoded, the ambiguity for GPS and GLONASS C/A code increases to 6,000 km. This distinction does not apply to other signals as their code repetition periods are greater than or equal to the data message symbol length.

Resolution of the ambiguity in pseudo-ranges differenced across satellites is relatively straightforward. Where an approximate position has been provided through acquisition aiding (see Section 10.5.1), this can be used to predict the differential pseudo-ranges and the ambiguity value that gives the closest match between measurements and predictions selected. If the user is stationary, an approximate position may also be calculated from the GNSS pseudo-range rates using Doppler positioning (Section 7.1.7) [70]. Other methods require the candidate ambiguities to be searched. With signals from five or more satellites, a consistency check can be applied, selecting the candidate least-squares navigation solution with the smallest weighted residual test statistic, determined using (10.21). With only four satellite signals, the solution must be constrained to within a certain distance of the Earth's surface.

However, this still leaves an ambiguity in the receiver clock bias and a corresponding common-mode ambiguity in the times of signal transmission. GNSS satellites move about 4m in a millisecond, so a timing error results in a satellite position error which, in turn, produces a user position error of around a meter per millisecond of timing error.

Resolving this common-mode timing ambiguity is more difficult as the candidate navigation solutions are much closer together. Signals from at least five satellites are required. Consistency checking may be performed with data averaged across several epochs. Alternatively, the ambiguity may be estimated as a state in the navigation solution [70] and then rounded to the nearest integer multiple of the code repetition interval once its uncertainty is sufficiently small (which may also require multiple epochs of data). Another method is to minimize the difference between the measured and predicted pseudo-range rates as a function of the transmission time. This is more accurate where the user can be assumed to be stationary [71].

G.13 GNSS Repeaters

The GNSS signal strength within buildings may be increased by retransmitting the signal inside the building. However, the user equipment will report its position as that of the retransmission system's receiving antenna. If the retransmitted signals are cycled between four antennas within the building, the user location can be determined from the pseudo-range jumps each time the signal switches antenna as these jumps are essentially TDOA measurements [72, 73]. Receiver modifications are not essential, though they can improve performance. An alternative, which does require receiver modification, is to retransmit from all antennas simultaneously, but with different time delays [74].

Because they are using the same PRN codes, all forms of GNSS retransmission cause much greater disruption to direct GNSS reception than pseudolite signals of the same strength. GNSS retransmission is illegal in many countries.

References

- [1] Aparicio, M., et al., "GPS Satellite and Payload," In *Global Positioning System: Theory and Applications Volume I*, B. W. Parkinson and J. J. Spilker, Jr., (eds.), Washington, DC: AIAA, 1996, pp. 209–244.
- [2] Spilker, J. J., Jr., "Signal Structure and Theoretical Performance," In *Global Positioning System: Theory and Applications Volume I*, B. W. Parkinson and J. J. Spilker, Jr., (eds.), Washington, DC: AIAA, 1996, pp. 57–119.

- [3] Fearheller, S., and R., Clark, "Other Satellite Navigation Systems," In *Understanding GPS Principles and Applications*, 2nd ed., E. D. Kaplan and C. J. Hegarty, (eds.), Norwood, MA: Artech House, 2006, pp. 595–634.
- [4] Revniviykh, S., et al., "GLONASS Ground Control Segment: Orbit, Clock, Time Scale and Geodesy Definition," *Proc. ION GNSS 2012*, Nashville, TN, September 2012.
- [5] Crop, O., *The European GNSS Programmes – Galileo Program Status*, European Commission Presentation, February 2011.
- [6] Dinwiddy, S. E., E. Breeuwer, and J. H. Hahn, "The Galileo System," *Proc. ENC-GNSS 2004*, Rotterdam, Netherlands, May 2004.
- [7] McDonald, K. D., "Early development of the global positioning system," In *Galileo: Europe's Guiding Star*, pp. 114–128, Blanchard, W. (ed), London, UK: Faircourt Ltd, 2006.
- [8] Parkinson, B. W., "Origins, Evolution, and Future of Satellite Navigation", *Journal of Guidance, Control and Dynamics*, Vol. 20. No. 1, 1997, pp. 11–25.
- [9] Parkinson, B. W., "Introduction and Heritage of NAVSTAR," In *Global Positioning System: Theory and Applications Volume I*, B. W. Parkinson, and J. J. Spilker, Jr., (eds.), Washington, DC: AIAA, 1996, pp. 3–28.
- [10] Parkinson, B. W., and S. T. Powers, "The Origins of GPS And the Pioneers Who Launched the System," *GPS World*, May 2010, pp. 30–41.
- [11] Parkinson, B. W., and S. T. Powers, "Fighting to Survive: Five Challenges, One Key Technology, the Political Battlefield – and a GPS Mafia," *GPS World*, June 2010, pp. 8–18.
- [12] Forssell, B. *Radionavigation Systems*, Norwood, MA: Artech House, 2008 (First Published 1991).
- [13] Van Graas, F., and M. S. Braasch, "Selective Availability," In *Global Positioning System: Theory and Applications Volume I*, B. W. Parkinson, and J. J. Spilker, Jr., (eds.), Washington, DC: AIAA, 1996, pp. 601–621.
- [14] Creel, T. et al, "New, Improved GPS: The Legacy Accuracy Improvement Initiative," *GPS World*, March 2006, pp. 20–31.
- [15] Kee, C., Parkinson, B. W., and Axelrad, P., "Wide Area Differential GPS," *Navigation: JION*, Vol. 38, No. 2, 1991, pp. 123–145.
- [16] Ashkenazi, V. et al., "Wide-Area Differential GPS: A Performance Study," *Navigation: JION*, Vol. 40, No. 3, 1993, pp. 297–319.
- [17] Braff, R., and C. Shively, "GPS Integrity Channel," *Navigation: JION*, Vol. 32, No. 4, 1985, pp. 334–350.
- [18] Braff, R., "Description of the FAA's Local Area Augmentation System (LAAS)," *Navigation: JION*, Vol. 44, No. 4, 1997, pp. 411–423.
- [19] Crosby, G. K., et al., "A Ground-based Regional Augmentation System (GRAS)- The Australian Proposal," *Proc. ION GPS 2000*, Salt Lake City, UT, September 2000, pp. 713–721.
- [20] Pratt, A. R., "New Navigation Signals and Future Systems in Evolution," In *GNSS Applications and Methods*, S. Gleason and D. Gebre-Egziabher, (eds.), Norwood, MA: Artech House, 2009, pp. 437–483.
- [21] Hein, G. W., et al., "MBOC: The New Optimized Spreading Modulation Recommended for GALILEO L1 OS and GPS L1C," *Proc. IEEE/ION PLANS*, San Diego, CA, April 2006, pp. 883–892.
- [22] Falcone, M., P. Erhard, and G. W. Hein, "Galileo," In *Understanding GPS Principles and Applications*, 2nd ed., E. D. Kaplan and C. J. Hegarty, (eds.), Norwood, MA: Artech House, 2006, pp. 559–594.
- [23] Kreher, J., *GALILEO Signals: RF Characteristics*, ICAO Navigation Systems Panel, Working Group of the Whole, Working Paper 36, October 2004.
- [24] Issler, J.-L., et al., "Spectral Measurements of GNSS Satellite Signals Need for Wide Transmitted Bands," *Proc. ION GPS/GNSS 2003*, Portland, OR, September 2003, pp. 445–460.

- [25] Lestarquit, L., G. Artaud, and J-L. Issler, "AltBOC for Dummies or Everything You Always Wanted to Know About AltBOC," *Proc. ION GNSS 2008*, Savannah, GA, September 2008, pp. 961–970.
- [26] Avila-Rodriguez, J. A., *On Generalized Signal Waveforms for Satellite Navigation*, PhD Thesis, University of the Federal Armed Forces, Munich, Germany, 2008.
- [27] Hodgart, M. S., "Galileo's Problem with PRS or What's in a Phase?," *International Journal of Navigation and Observation*, 2011, Article ID 247360.
- [28] Anon., *Navstar GPS Space Segment/ Navigation User Interfaces*, IS-GPS-200, Revision F, GPS Directorate, September 2011.
- [29] Anon., *Navstar GPS Space Segment/ User Segment L5 Interfaces*, IS-GPS-705, Revision B, GPS Directorate, September 2011.
- [30] Anon., *Navstar GPS Space Segment/ User Segment L1C Interface*, IS-GPS-800, Revision B, GPS Directorate, September 2011.
- [31] Anon., *Global Navigation Satellite System GLONASS Interface Control Document*, Edition 5.1, Russian Institute of Space Device Engineering, 2008.
- [32] Urlichich, Y., et al., "GLONASS Developing Strategy," *Proc. ION GNSS 2010*, Portland, OR, September 2010, pp. 1566–1571.
- [33] Anon., *European GNSS (Galileo) Open Service Signal in Space Interface Control Document*, Issue 1 Revision 1, GNSS Supervisory Authority, September 2010.
- [34] Stewart, M., and M. Tsakiri, "GLONASS Broadcast Orbit Computation," *GPS Solutions*, Vol. 2, No. 2, 1998, pp. 16–27.
- [35] Ashby, N., and J. J. Spilker, Jr., "Introduction to Relativistic Effects on the Global Positioning System," In *Global Positioning System: Theory and Applications Volume I*, B. W. Parkinson and J. J. Spilker, Jr., (eds.), Washington, DC: AIAA, 1996, pp. 623–697.
- [36] Rindler, W., *Essential Relativity: Special, General, and Cosmological*, 2nd ed., New York: Springer-Verlag, 1977.
- [37] Blunt, P. D., "GNSS Signal Acquisition and Tracking," In *GNSS Applications and Methods*, S. Gleason and D. Gebre-Egziabher, (eds), Norwood, MA: Artech House, 2009, pp. 23–54.
- [38] Hodgart, M. S., and P. D. Blunt, "Dual Estimate Receiver of Binary Offset Carrier Modulated Signals for Global Navigation Satellite Systems," *Electronics Letters*, Vol. 43, No. 16, 2007, pp. 877–878.
- [39] Hodgart, M. S., P. D. Blunt, and M. Unwin "Double Estimator: A New Receiver for Tracking BOC Signals," *Inside GNSS*, Spring 2008, pp. 26–36.
- [40] Blunt, P. D., *Advanced Global Navigation Satellite System Receiver Design*, PhD Thesis, University of Surrey, 2007.
- [41] Hodgart, M. S., R. M. Weiler, and M. Unwin, "A Triple Estimating Receiver of Multiplexed Binary Offset Carrier (MBOC) Modulated Signals," *Proc. ION GNSS 2008*, Savannah, GA, September 2008, pp. 877–886.
- [42] Fine, P., and W. Wilson, "Tracking Algorithm for GPS Offset Carrier Signals," *Proc. ION NTM*, San Diego, CA, January 1999, pp. 671–676.
- [43] Fante, R.L., "Unambiguous Tracker for GPS Binary-Offset-Carrier Signals," *Proc. ION 59th AM*, Albuquerque, NM, June 2003, pp. 141–145.
- [44] Dovis, F., P. Mulassano, and L. Lo Presti, "A Novel Algorithm for the Code Tracking of BOC(n,n) Modulated Signals," *Proc. ION GNSS 2005*, Long Beach, CA, September 2005, pp. 152–155.
- [45] Julien, O., et al., "ASPeCT: Unambiguous Sine-BOC(n,n) Acquisition/Tracking Technique for Navigation Applications," *IEEE. Trans. on AES*, Vol. 43, No. 1, 2007, pp. 150–162.
- [46] Yao, Z., "A New Unambiguous Tracking Technique for Sine-BOC(2n,n) Signals," *Proc. ION GNSS 2008*, Savannah, GA, September 2008, pp. 1490–1496.

- [47] Kiesel, S., et al., "Discriminator Weighting and Performance of a Deeply Coupled GPS/INS System at low CN0," *Proc. ION ITM*, San Diego, CA, January 2011, pp. 858–867.
- [48] Betz, J. W., "Effect of Partial-Band Interference on Receiver Estimation of C/N0: Theory," *Proc. ION NTM*, Long Beach, CA, January 2001, pp. 817–828.
- [49] Ross, J. T., J. L. Leva, and S. Yoder, "Effect of Partial-Band Interference on Receiver Estimation of C/N0: Measurements," *Proc. ION NTM*, Long Beach, CA, January 2001, pp. 829–838.
- [50] Groves, P. D., "GPS Signal to Noise Measurement in Weak Signal and High Interference Environments," *Navigation: JION*, Vol. 52, No. 2, 2005, pp. 83–92.
- [51] Falletti, E., M. Pini, and L. Lo Pesti, "Low Complexity Carrier-to-Noise Ratio Estimators for GNSS Digital Receivers," *IEEE. Trans. on AES*, Vol. 47, No. 1, 2011, pp. 420–437.
- [52] Muthuraman, K., and D. Borio, "C/N₀ Estimation for Modernized GNSS Signals: Theoretical Bounds and a Novel Iterative Estimator," *Navigation: JION*, Vol. 57, No. 4, 2010, pp. 309–323.
- [53] Tetewsky, A., et al., "Making Sense of Inter-Signal Corrections," *Inside GNSS*, July/August 2009, pp. 37–47.
- [54] Klobuchar, J. A., "Ionosphere Effects on GPS," In *Global Positioning System: Theory and Applications Volume I*, B. W. Parkinson and J. J. Spilker, Jr., (eds.), Washington, DC: AIAA, 1996, pp. 485–515.
- [55] Misra, P., and P. Enge, *Global Positioning System Signals, Measurements, and Performance*, 2nd ed., Lincoln, MA: Ganga-Jamuna Press, 2006.
- [56] Collins, J. P., *Assessment and Development of a Tropospheric Delay Model for Aircraft Users of the Global Positioning System*, Technical Report No. 203, University of New Brunswick, September 1999.
- [57] Conley, R., et al., "Performance of Stand-Alone GPS," In *Understanding GPS Principles and Applications*, 2nd ed., E. D. Kaplan and C. J. Hegarty, (eds.), Norwood, MA: Artech House, 2006, pp. 301–378.
- [58] Juang, J.-C., "On Solving the Multi-constellation Pseudorange Equations," *Navigation: JION*, Vol. 57, No. 3, 2010, pp. 201–212.
- [59] Chan, F.-C., and B. Pervan, "High-Integrity GPS/INS Integrated Navigation with Error Detection and Application to LAAS," *Journal of Navigation*, Vol. 64, No. 3, 2011, pp. 467–493.
- [60] Teunissen, P. J. G., "Least Squares Estimation of Integer GPS Ambiguities," *Proc. International Association of Geodesy General Meeting*, Beijing, China, August 1993.
- [61] Teunissen, P. J. G., P. J. De Jonge, and C. C. J. M. Tiberius, "Performance of the LAMBDA Method for Fast GPS Ambiguity Resolution," *Navigation: JION*, Vol. 44, No. 3, 1997, pp. 373–383.
- [62] De Jonge, P., and C. Tiberius, *The LAMBDA Method for Integer Ambiguity Estimation: Implementation Aspects*, Delft University of Technology, report no. LGR 12, 1996.
- [63] Sennott, J. W., and D. Senffner, "Navigation Receiver with Coupled Signal-Tracking Channels," U.S. Patent 5,343,209, 1994.
- [64] Abbott, A. S. and Lillo, W. E., "Global Positioning System and Inertial Measuring Unit Ultra-tight Coupling Method," U.S. Patent 6,916,025, 2003.
- [65] Axelrad, P., et al., "Collective Detection and Direct Positioning Using Multiple GNSS Satellites," *Navigation: JION*, Vol. 58, No. 4, 2011, pp. 305–321.
- [66] Reichert, A. K., and P. Axelrad, "Carrier-Phase Multipath Corrections for GPS-based Satellite Attitude Determination," *Navigation: JION*, Vol. 48, No. 2, 2001, pp. 77–88.
- [67] Hodgart, S., and R. Wong, "Statistically Optimized In-Flight Estimation of GPS Carrier Phase Multipath for LEO Satellite Attitude Determination," *Navigation: JION*, Vol. 53, No. 3, 2006, pp. 181–202.
- [68] Thornberg, D. B., et al., "LAAS Integrated Multipath-Limiting Antenna," *Navigation: JION*, Vol. 50, No. 2, 2003, pp. 117–130.

- [69] Lau, L., “Comparison of Measurement and Position Domain Multipath Filtering Techniques with the Repeatable GPS Orbits for Static Antennas,” *Survey Review*, Vol. 44, No. 324., 2012, pp. 9–16.
- [70] Van Diggelen, F., *A-GPS: Assisted GPS, GNSS, and SBAS*, Norwood, MA: Artech House, 2009.
- [71] Sheynblat, L., and J. C. Scheller, Jr., “Method and Apparatus for Determining Time in a Satellite Positioning System,” U.S. patent 6,215,442, filed 1997, granted 2001.
- [72] Caratori, J., et al., “UPGRADE RnS Indoor Positioning System in an Office Building,” *Proc. ION GNSS 2004*, Long Beach, CA, September 2004, pp. 1959–1969.
- [73] Jee, H.-I., S.-H. Choi, and S.-C. Bu, “Indoor Positioning using TDOA Measurements from Switching GPS Repeater,” *Proc. ION GNSS 2004*, Long Beach, CA, September 2004, pp. 1970–1976.
- [74] Im, S.-H., and G.-I. Jee, “Feasibility Study of Pseudolite Techniques Using Signal Transmission Delay and Code Offset,” *Proc. ION ITM*, Anaheim, CA, January 2009, pp. 798–803.